# Disclaimer

The report at hand was written in the course of the respective class at the University of Bonn. If not stated differently on top of the first page or the following website, the report was prepared and handed in solely by me, Marvin Zanke. Any handwritten annotations are usually corrections that I or a tutor made. For more information and all my material, check: https://www.physics-and-stuff.com/

**I raise no claim to correctness and completeness of the given report! This equally applies to the corrections mentioned above.**

This work by Marvin Zanke is licensed under a Creative Commons Attribution-NonCommercial-ShareAlike 4.0 International License.

# Advanced Laboratory Course

**E213: Analysis of decays of heavy vector boson $Z^0$**

**Group P8**

Marvin Zanke
s6mazank@uni-bonn.de

Fabian Müller
s6fnmuel@uni-bonn.de

August 09/10, 2018

# Contents

# Abstract

In this experiment, we consider the $Z^0$ boson and its decay channels $e^-e^+$, $\mu^-\mu^+$, $\tau^-\tau^+$ and $q\bar{q}$. We use data from the OPAL detector in the $e^-e^+$ collider LEP at CERN in order to find different properties of the $Z^0$ boson. To do so, we will also use Monte Carlo generated data samples. These allow us to find criteria to distinguish between the possible final state events, either by a graphical analysis of the detectors response, or by a statistical analysis relying on a set of variables such as the deposited energy in the calorimeters.

The experiment is carried out on two days and divided into two parts. While in the first part, we analyze the events graphically and find out how to distinguish the tracks of different decay channels, the second part focuses on a statistical analysis of a huge OPAL data set. To this end, we need to find cuts on a tuple of variables using Monte Carlo generated samples, making the ascription to the channels possible without a graphical analysis but rather with an algorithm.

Among other things, we will obtain the Weinberg angle, the mass and decay width of the $Z^0$ boson and also check lepton universality as well as determine the number of light neutrino generations from and with the huge OPAL data set.

# 1 Theory

If not mentioned explicitly, the theory is based on the references [1] and [2].

## 1.1 Elementary Particles and the Standard Model

As far as we understand nowadays, most of the physics in our universe can be described with the help of a few *elementary particles*, collected in the so-called *standard model*, whose content is depicted in figure 1.1. Note here, that the gravitation is not taken into account because it is weak compared to the other forces. One easily verifies, that these elementary particles can be separated into *fermions* with spin $\frac{1}{2}$ and *bosons* with spin 1. The fermionic part is made up out of quarks and leptons – also referred to as the *matter content* – whereas the bosonic part is made up out of the vector bosons, mediating the electromagnetic-, weak-, and strong force between the particles and the higgs boson. As indicated in the figure, there exists an anti-particle for each particle, having the same mass but carrying the opposite charge. The whole theory is consistent only as a field theory of quanta, i.e. a quantum field theory.

Interactions in quantum field theories often rely on the principle of *local gauge invariance*. One promotes a global gauge symmetry of the Lagrangian to a local one and demands invariance, which in turn gives rise to the need of introducing gauge bosons. The gauge bosons couple to matter in (non-&)abelian-gauge theories and additionally to other gauge bosons in non-abelian gauge theories. Abelian and non-abelian refers to the underlying symmetry group and its generators here.

For the standard model, one chooses the most convenient and successful choice of an *electroweak unifying theory*, $SU(3)_{\mathrm{C}} \times SU(2)_{\mathrm{L}} \times U(1)_{\mathrm{Y}}$, where 'C' refers to color, 'L' to left-handed, 'Y' to the hypercharge. The first group then implies the existence of *eight gluons* and a coupling to particles carrying color, while the second group implies the existence of *three gauge bosons* $(W^+, W^0, W^-)$ and a coupling to particles carrying weak charge. The third group gives rise to *one gauge boson* $B$

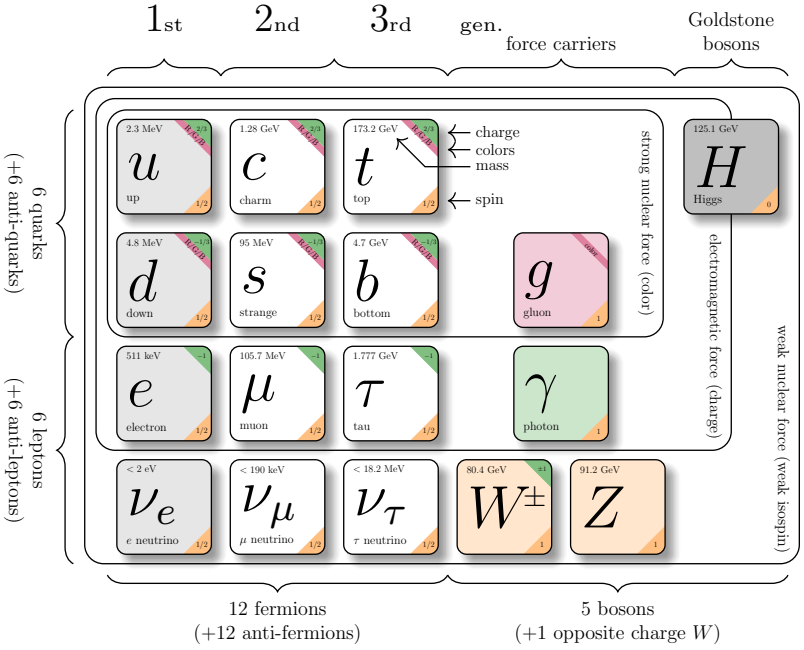


Figure 1.1.: The matter and gauge content of the Standard Model. (Code created in TikZ by Carsten Burgard, taken from [3], slightly edited for our purpose).

that couples via the hypercharge $Y = Q - I_3$, where $Q$ is the charge and $I_3$ the third component of the weak isospin. The particles are here assumed to be written down as *doublets or singlets* under $SU(2)_\mathrm{L}$, e.g.

$$\begin{pmatrix} \nu_e \\ e^- \end{pmatrix}_\mathrm{L}, \qquad \begin{pmatrix} u \\ d \end{pmatrix}_\mathrm{L}$$

or

$$e^-_\mathrm{R}, \qquad u_\mathrm{R}, \qquad d_\mathrm{R}$$

respectively for the first generation. The color-indices are suppressed, as obviously, the quarks would consist of three different color-states. Note here, that right-handed neutrinos do not exist in the standard model and 'have to be' included via an extension as so-called physics beyond the standard model.

For reasons of consistency to experiments, the physical photon and $Z^0$ have to be a superposition of $B$ and $W^0$ respectively, defining the *Weinberg angle* $\theta$ as the mixing angle for these. The gluons, as well as the $W^+$ and $W^-$ are consistent with the physical observed bosons. Furthermore, the $SU(3)_\mathrm{C} \times SU(2)_\mathrm{L} \times U(1)_\mathrm{Y}$ gauge

group introduces three different couplings into the theory, which, after performing the change of basis indicated above, represent the electric charge $e$ as the coupling constant of QED, the weak coupling and the strong coupling. With the help of the formalism of quantum field theory, one can show that the coupling of QED increases (decreases) with increasing (decreasing) momenta, while the strong coupling constant increases (decreases) with decreasing (increasing) momenta. This leads to the phenomenon of *asymptotic freedom*, stating that quarks behave like free particles for large probed energies, while they only appear in colorless bound states, being referred to as *confinement*. These color-neutral hadrons can form so-called *jets* when they are emitted as bundles in scatter or decay processes.

Up to this point, the gauge bosons are massless. A mass term for these would violate the gauge symmetry and is thus forbidden. Instead, one generates masses via the *higgs mechanism*. The group $SU(2)_{\mathrm{L}} \times U(1)_{\mathrm{Y}}$ is *spontaneously broken* to $U(1)_{\mathrm{em}}$ with the help of a complex higgs doublet $(h^+, h^0)$ that acquires its *vacuum expectation value*, e.g. $(0, v)$. Note here that the four degrees of freedom from the initial higgs doublet are reduced to one and those three missing degrees of freedom are absorbed by three of the former massless gauge bosons – massive particles have an additional longitudinal polarization in contrast to massless ones. Consistent with Goldstones theorem, we get one massless gauge boson which we identify with the photon and three massive, the $(W^+, W^-)$ and $Z^0$.

Masses for fermions can be introduced via *Yukawa couplings*, which couple the higgs doublet to the fermions and give rise to mass terms after having the higgs doublet acquire its vacuum expectation value.

This is of course only a short summary and presumes that the reader has some basic knowledge of those concepts. For more details, we can recommend the summary in [4, p. 161 et sqq.] on which this recap is partly based on. For a deeper understanding of quantum field theory, we refer to [5].

## 1.2 $e^-e^+$ Interactions near $M_Z$

In *electron-positron interactions at LEP*, electrons and positrons are accelerated and brought to collision. For this process, the following interactions can be observed:

- scattering of $e^-e^+$ producing a fermion-antifermion pair, see figure 1.2.
- elastic scattering of $e^-e^+$ via $s$- and $t$-channel by photon or $Z^0$ exchange, see figure 1.3.

- annihilation of $e^-e^+$ into two or more real photons, see figure 1.4
- production of virtual photons or $Z^0$ bosons, one from $e^-$, the other from $e^+$, which then interact and produce fermion-antifermion pairs, e.g. hadrons.

If the experiment is carried out close to the $Z^0$ mass, the final state can not contain top-quarks because of their large mass.

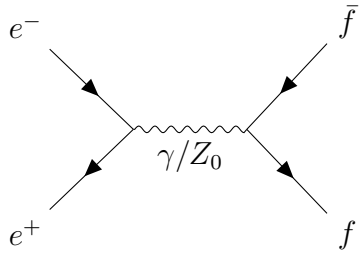


Figure 1.2.: Inelastic $e^-e^+$ scattering.

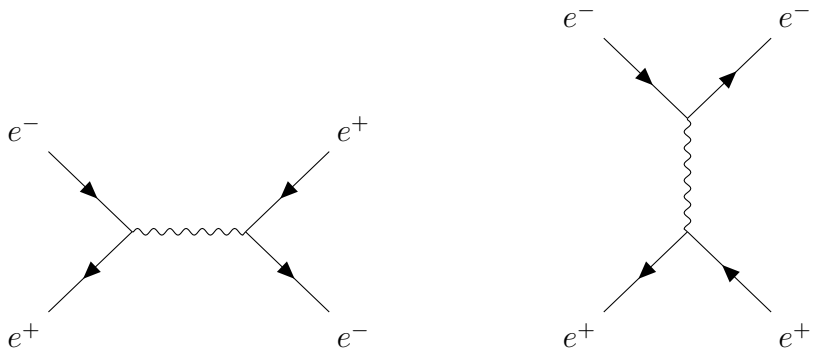


Figure 1.3.: Elastic $e^-e^+$ scattering. Left: $s$-channel. Right: $t$-channel.

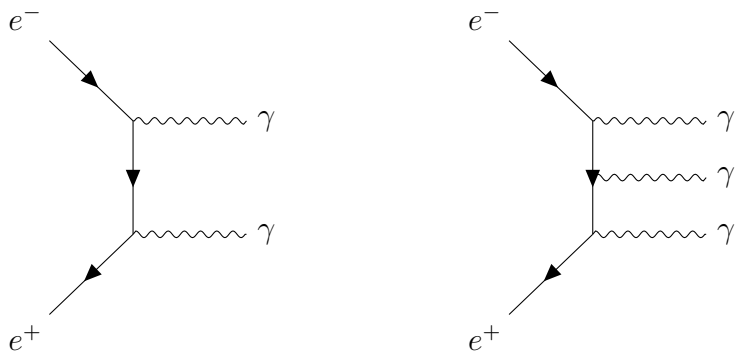


Figure 1.4.: Annihilation of $e^-e^+$ into real photons.

The standard model predicts the cross section of $e^-e^+$-annihilation with the final states mainly being lepton-antilepton- or quark-antiquark-pairs. Quarks (and

gluons) never appear as free states though and as a consequence have to *hadronize*, i.e. form colorless hadrons. Here, close to the $Z^0$ *resonance*, the cross section of $e^-e^+ \to f\bar{f}$ is dominated by the $Z^0$ part. Using the *partial width* of the $Z^0$ boson into the fermions $f$:

$$\Gamma_f = \frac{\sqrt{2}N_C^f}{12\pi} G_F M_Z^3 \left((g_V^f)^2 + (g_A^f)^2\right) \tag{1.1}$$

where

$$\begin{aligned} G_\mathrm{F} &= 1.1663 \times 10^{-5}\,\mathrm{GeV}^{-2}, & g_V^f &= I_3^f - 2Q_f \sin^2\theta_\mathrm{W}, \\ M_Z &= 91.18\,\mathrm{GeV}, & g_A^f &= I_3^f, \\ \sin^2\theta_\mathrm{W} &= 0.2312 \end{aligned} \tag{1.2}$$

with $I_3^f$ the third component of the weak isospin and $Q_f$ the charge in units of the elementary charge $e$, the *cross section* close to the peak can be written as

$$\sigma_f^\mathrm{peak} = \frac{12\pi}{M_Z^2} \frac{\Gamma_\mathrm{e}\Gamma_f}{\Gamma_Z^2}. \tag{1.3}$$

The *differential cross section* of $e^-e^+ \to f\bar{f}$ in lowest order pertubation theory – now including the $Z^0$ and photon as intermediate states – is given by:

$$\frac{\mathrm{d}\sigma_f}{\mathrm{d}\Omega} = \frac{\alpha^2 N_c^f}{4s} \left(F_1(s)(1+\cos^2(\theta)) + 2F_2(s)\cos(\theta)\right) \tag{1.4}$$

where

$$\begin{aligned} F_1(s) &= Q_f^2 - 2v_e v_f Q_f \Re(\chi(s)) + (v_e^2 + a_e^2)(v_f^2 + a_f^2)|\chi(s)|^2, \\ F_2(s) &= -2a_e a_f Q_f \Re(\chi(s)) + 4v_e a_e v_f a_f \chi(s)|^2, \\ v_f &= g_V^f/(2\sin(\theta_W)\cos(\theta_W)), \\ a_f &= g_A^f/(2\sin(\theta_W)\cos(\theta_W)), \\ \chi(s) &= s/((s - M_Z^2) + \mathrm{i}\, s\Gamma_Z/M_Z). \end{aligned}$$

For the final state being $e^-e^+$, there is a t-channel in addition to the s-channel. The behavior of the s-channel is $\mathrm{d}\sigma_s/\mathrm{d}\Omega \propto (1+\cos^2\theta)$, while the t-channel behaves like $\mathrm{d}\sigma_t/\mathrm{d}\Omega \propto (1-\cos\theta)^{-2}$.

The cross section in eq. (1.4) exhibits an asymmetry in forward-backward direc-

tion. This behavior is quantified in the forward-backward asymmetry $A_{\mathrm{FB}}$:

$$A_{\mathrm{FB}} = \frac{\int_0^1 \frac{\mathrm{d}\sigma}{\mathrm{d}\cos(\theta)}\mathrm{d}\cos(\theta) - \int_{-1}^0 \frac{\mathrm{d}\sigma}{\mathrm{d}\cos(\theta)}\mathrm{d}\cos(\theta)}{\int_{-1}^1 \frac{\mathrm{d}\sigma}{\mathrm{d}\cos(\theta)}\mathrm{d}\cos(\theta)} = \frac{3}{4}\frac{F_2}{F_1}. \tag{1.5}$$

For leptons, this can be approximated at $s = M_Z^2$ by

$$A_{\mathrm{FB}}^{l,\mathrm{peak}} \approx 3\left(\frac{v_l}{a_l}\right)^2 = 3(1 - 4\sin^2\theta_W)^2. \tag{1.6}$$

In order to make precise predictions in high energy experiments *radiative corrections* have to be taken into account. These correspond to higher order Feynman diagrams. One distinguishes between *real and virtual corrections*. In real corrections a photon or a gluon is emmited in the initial or final state, whereas virtual corrections contain loops inside the diagram. Figure 1.5 shows some examples.
These corrections modify the shape of the cross section slightly. E.g. inital state radiation leads to a reduced centre-of-mass energy, moving the peak in the resonance curve.

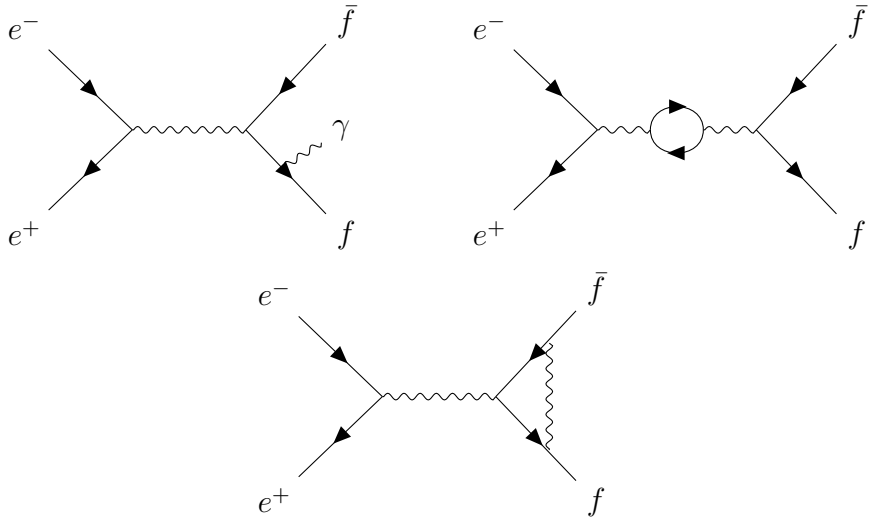


Figure 1.5.: Radiative corrections to (inelastic) $e^-e^+$ scattering. The upper left diagram shows bremsstrahlung in the final states. The other two diagrams show virtual corrections.

## 1.3 Luminosity

Having obtained the experimentally observed event rates for a process, one is interested in calculating the cross section $\sigma$. This can be done with the help of the so-called *luminosity* $L$, which in turn can be obtained by simultaneously measuring the rate of another process with known cross section. In $e^-e^+$ storage ring experiments, this is done by bhabha scattering. For the event rate $\mathrm{d}n/\mathrm{d}t$, we then have

$$\frac{\mathrm{d}n}{\mathrm{d}t} = \sigma \cdot L,$$

or equivalently

$$n = \sigma \int L \,\mathrm{d}t \tag{1.7}$$

with the integrated luminosity $\mathcal{L} = \int L \,\mathrm{d}t$.

## 1.4 The OPAL Experiment

### 1.4.1 Detector Components

Modern detector systems usually use combinations of *drift chambers*, to monitor the track and to measure the momentum of charged particles and *calorimeters*, measuring the energy of charged and neutral particles.

The functionality of drift chambers is based on *proportional counters*, which are gas-filled volumes with positively charged wires aligned in it. An electron liberated by ionization of an incoming charged particle will drift towards this wire. Due to the gain of energy in the electric field, an avalanche of electrons and ions will be created, leading to a signal on the wire. Using multi wire proportional counters and assuming a constant drift time, the trajectory of charged particles can be reconstructed by measuring the time difference between entry of the particle and response of the specific wire.

The *jet chamber* is a special type of a drift chamber, having a good spatial resolution and thus being able to resolve double trajectories, making it a useful detector for hadronic events. There are more types of drift chambers, such as the *time projection chamber*, all having special functions and differing (slightly) in their components. Going into more detail here would go way beyond the scope of this report.

In *calorimeters*, incoming particles deposit their energy via electromagnetic and strong interactions, leading to particle showers and producing a proportional signal. They are often constructed in layers of dense absorbers and active detection devices such as scintillators.

Electrons passing matter create a *shower* by the combined effects of *bremsstrahlung* and *pair production*. Reaching a critical energy where the energy loss of bremsstrahlung is equal to ionization, the shower stops. The radiation length $X_0$ is an important characteristic of these showers. It describes the mean distance after which the particle content of the shower doubles.

Incoming hadrons produce *showers* by inelastic nucleon collisions until the shower hadrons are absorbed or completely slowed down. Due to the large masses, bremsstrahlung does not play an important role here. Part of the energy will be shared among neutrinos and the creation of muon pairs, which do not interact/are not absorbed and thus is lost for ionization. The length of such a hadronic shower is characterized by the nuclear absorption length $\lambda_0$.

### 1.4.2 The OPAL-Detector

The schematic structure of the OPAL-detector is shown in figure 1.6. In the following, the layers are described from inner, surrounding the collision point, to outermost.

The *microvertex detector* is a silicon detector designed to give information on the primary interactions. It is surrounded by the *vertex chamber*, a multiwire proportional counter used for tracking of the created particles, followed by the *jet chamber*, which simultaneously measures the energy loss. The $z$-resolution (see figure) is improved by the *Z-chambers*. This tank is enclosed by a solenoid followed by the *time-of-flight system*, triggering the detector and measuring the particles flight time. The construction is completed by the calorimeters. The *electromagnetic calorimeter (ECAL)* consists of lead glass blocks covering 98% of the solid angle, its endcaps contain a forward detector – *FCAL* – which is used to measure Bhabha scattering. The *hadronic calorimeter (HCAL)* has a sandwich construction of lead and detector material. Since muons pass through the ECAL and HCAL without much interaction, a so-called *muon chamber* detects produced muons.

### 1.4.3 Event Identification

The elements of the OPAL detector allow to distinguish between the different final states of the collision.

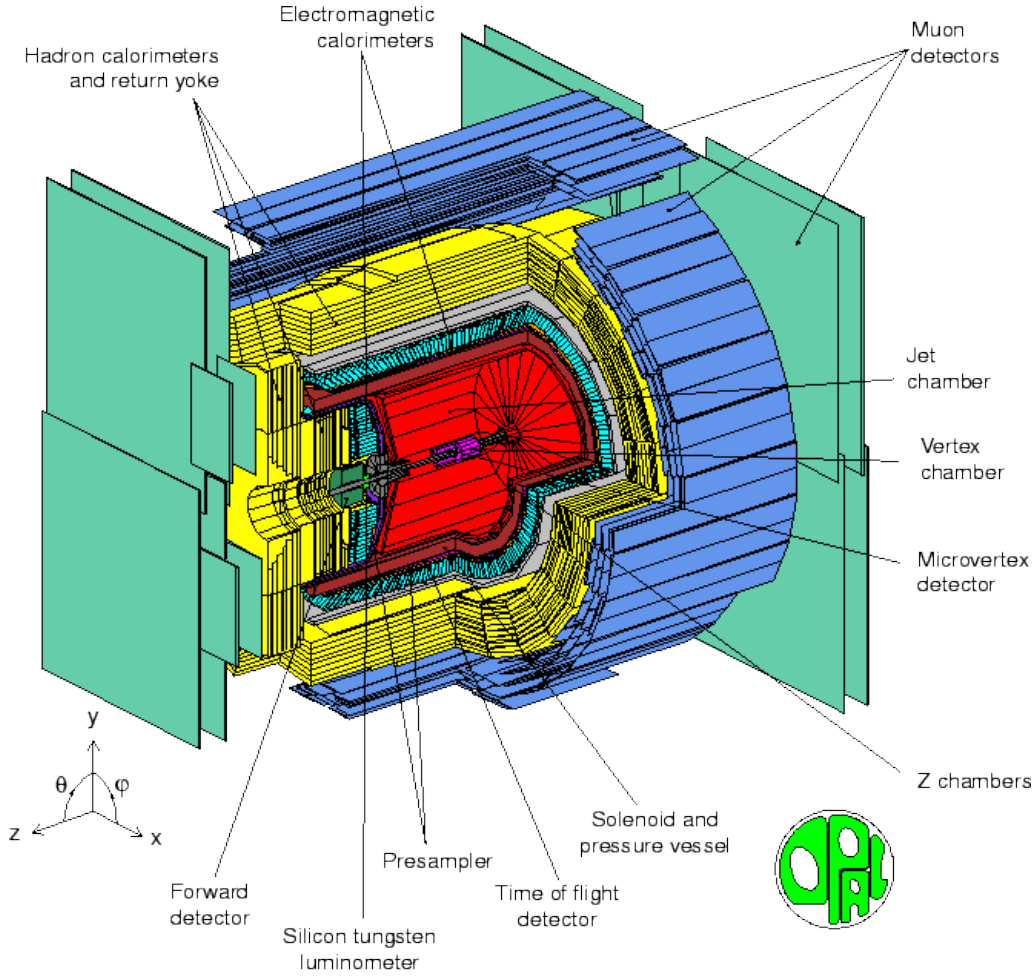


Figure 1.6.: Structure of the OPAL-detector, taken from [2].

An $e^-e^+$ event can be identified by two collinear tracks, which completely deposit their energy in the ECAL. In contrast, muons are detected in the muon chamber, as they almost lose no energy in the calorimeters. The tauon is short lived, so only the decay products can be observed. Typical for the tauon are one or three charged tracks. The leptonic events all have in common that they show a small multiplicity compared to $q\bar{q}$ events. Here, the quarks hadronize. The number of charged tracks and the energy deposited in the calorimeters is much greater than for leptonic events. The showers induced by these hadron jets, in contrast to the electromagnetic, start later and extend into the HCAL. With 88 %, the $q\bar{q}$ final state dominates the observed events. Neutrino events cannot be measured.

Figure 1.7 schematically shows the signature of different particles in the different layers of the detector. In the experiment, cuts in the number of tracks and the energies measured in the ECAL and HCAL will be used to identify the events. This and also the difference between the detector signals for different events shall become

much clearer later, during the analysis in this report.

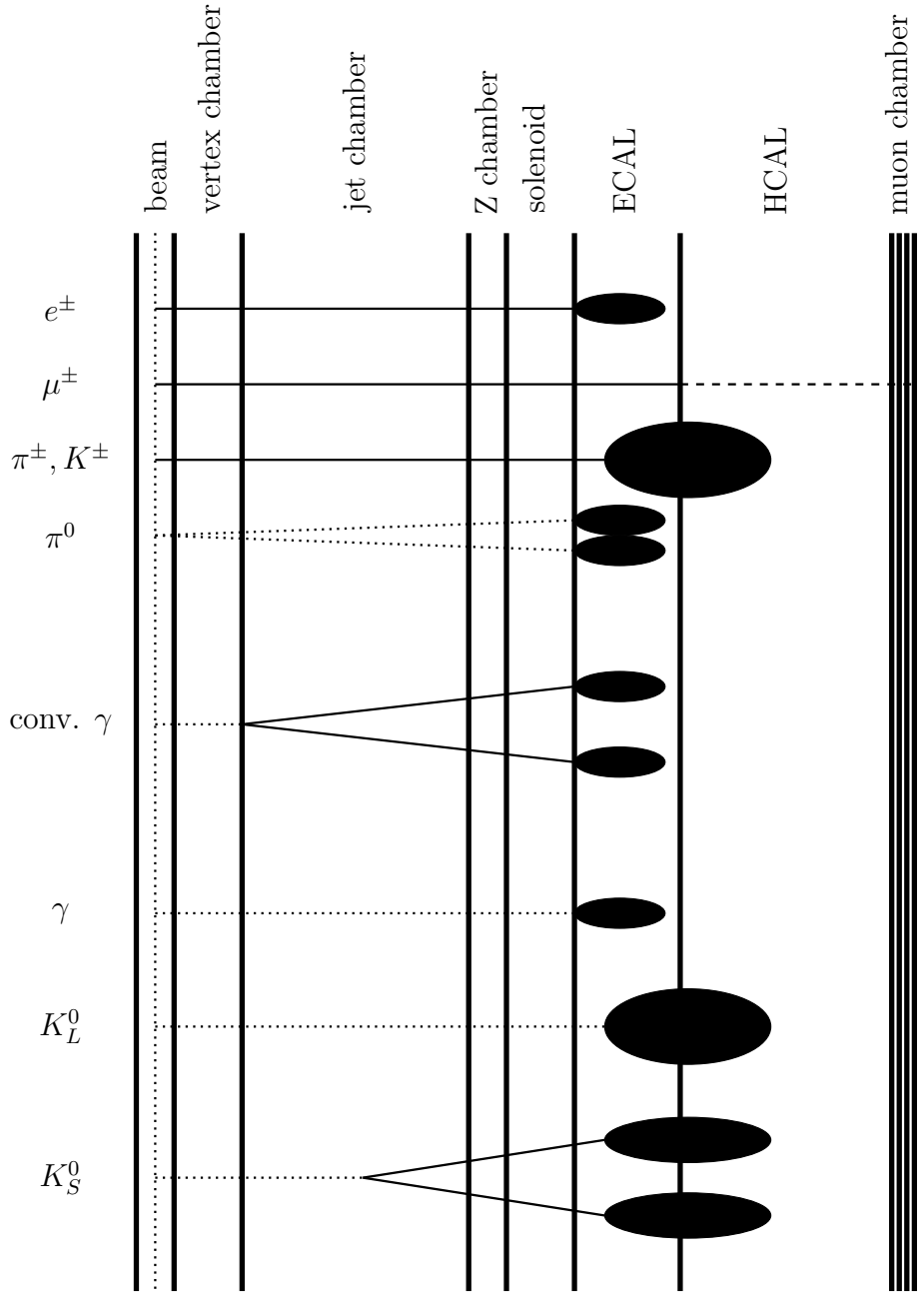


Figure 1.7.: Characteristic traces of particles at the OPAL detector. Solid lines depict the track of charged particles, dashed lines untrackable neutral particles. Bubbles represent the showers. (Reconstruction of [2])

## 1.5 Preliminary Tasks

**P.1:** *Calculate the decay width $\Gamma_f$ for the decays $Z^0 \to e^-e^+, \mu^-\mu^+, \tau^-\tau^+$ and hadrons and compare your result with the values from [2].*

| | $I_3^f$ | $Q_f$/e | $\Gamma_f$/MeV | $\Gamma_{f,\text{lit}}$/MeV, $[2, p.9]$ |
|---|---|---|---|---|
| $e, \mu, \tau$ | $-\frac{1}{2}$ | $-1$ | 83.4 | 83.8 |
| $\nu_\text{e}, \nu_\mu, \nu_\tau$ | $\frac{1}{2}$ | 0 | 165.8 | 167.6 |
| $u, c$ | $\frac{1}{2}$ | $\frac{2}{3}$ | 285.3 | 299.0 |
| $d, s, b$ | $-\frac{1}{2}$ | $-\frac{1}{3}$ | 367.8 | 378.0 |

Table 1.1.: The values of $I_3^f$ and $Q_f$ for the different families of leptons and quarks, as well as the calculated and literature decay widths. Note here, that we neglected the top-quark due to its large mass.

Using eq. (1.1) and eqs. (1.2), as well as the values for $I_3^f$ and $Q_f$ in table 1.1, we find the corresponding decay widths. Here, $N_C^f = 3$ for quarks and $N_C^f = 1$ for leptons has been used.

**P.2:** *Calculate the total $Z^0$ decay width, the hadronic decay width, the 'charged' leptonic decay width, the 'neutral' (invisible) lepton decay width and the partial cross sections at the maximum of the resonance.*

In order to determine the total $Z^0$ decay width, we calculate and then add up all the other contributions to the $Z^0$ decay width. To start with the hadronic decay width, we note that we have to add up the $u-$, $c-$ and $d-$, $s-$, $b-$quark contributions. Because of the large mass of the top-quark, it is neglected here. We then find

$$\Gamma_\text{hadronic} = 1674.08\,\text{MeV}.$$

For the decay width of the charged leptons, we proceed analogously, adding up the contributions from $e$, $\mu$ and $\tau$, yielding

$$\Gamma_\text{ch. leptons} = 250.2\,\text{MeV}.$$

For the neutral leptons, one finds

$$\Gamma_\text{neutr. leptons} = 497.52\,\text{MeV}.$$

Neutrinos are 'invisible' for the detector, as they interact only weakly.

In total, we then find

$$\Gamma_{Z^0} = \Gamma_{\text{hadronic}} + \Gamma_{\text{ch. leptons}} + \Gamma_{\text{neutr. leptons}} = 2421.80\,\text{MeV}.$$

For the partial cross sections at the maximum of the resonance, we make use of eq. (1.3). Here, we note that $\left[\sigma_f^{\text{peak}}\right] = 1/GeV^2 (= m^2)$ such that with $\hbar c = 0.197\,\text{GeV}\cdot\text{fm}$ and $1\,\text{b} = 100\,\text{fm}^2$ we have the corresponding conversion factors and find table 1.2. The left table gives the cross section for one separate particle, while the right table is the sum of the different species analogous to the previous task.

| | $\sigma_f^{\text{peak}}$/nb |
|---|---|
| charged lepton | 2.09 |
| neutral lepton | 4.15 |
| u-like quark | 7.14 |
| d-like quark | 9.20 |

| | $\sigma_{\Sigma f}^{\text{peak}}$/nb |
|---|---|
| charged leptons | 6.26 |
| neutral leptons | 12.45 |
| hadrons | 41.89 |
| total | 60.59 |

Table 1.2.: The (partial) cross sections near the maximum of the resonance for individual leptons/quarks (left) and for the sum of different species (right).

**P.3:** *Imagine that the decay into an additional pair of light fermions $(u, d, e, \nu)$ is possible. What would be the change (in percent) of the width of the $Z^0$ resonance curve?*

If the decay into an additional pair of light fermions was possible, the change (in %) of the width of the $Z^0$ resonance curve can be calculated via

$$C = \frac{\Gamma_{\text{add}}}{\Gamma_Z},$$

where $\Gamma_Z$ is the original $Z^0$ decay width and $\Gamma_{\text{add}}$ the additional decay width taken from table 1.1. The resulting changes as well as the total change upon adding one of each are given in table 1.3.

**P.4:** *Draw the expected angular distribution for the processes $e^-e^+ \to e^-e^+$ and $e^-e^+ \to \mu^-\mu^+$ . In the case of $e^-e^+ \to e^-e^+$ also plot the different contributions.*

The cross section for the reaction $e^-e^+ \to \mu^-\mu^+$ is given by eq. (1.4). A plot can be found in figure 1.8. For the reaction $e^-e^+ \to e^-e^+$, also the $t$-channel has to be included. The complicated cross section can be found in appendix A. Figure 1.9 shows its angular dependence and the different contributions.

| | $C$ in % |
|---|---|
| $u$ | 11.8 |
| $d$ | 15.2 |
| $e$ | 3.4 |
| $\nu$ | 6.9 |
| total | 37.3 |

Table 1.3.: The change in the decay width upon adding an additional pair of light fermions ($u$, $d$, $e$, $\nu$) and the total change on adding all of them.

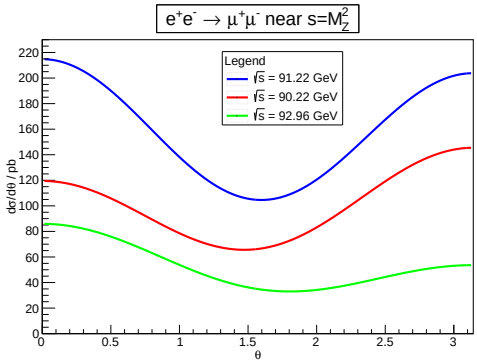


Figure 1.8.: Differential cross section for $e^-e^+ \to \mu^-\mu^+$.

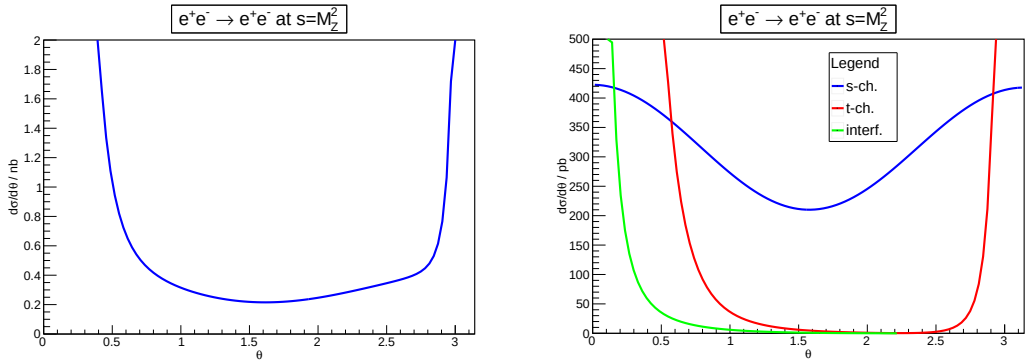


Figure 1.9.: Differential cross section for $e^-e^+ \to e^-e^+$. Left: Total cross section. Right: Contributions from different channels and the interference term.

**P.5:** *Calculate the forward-backward asymmetry in the process* $e^-e^+ \to \mu^-\mu^+$ *at* $\sqrt{s} = 91.225\,\text{GeV}$, $89.225\,\text{GeV}$ *and* $93.225\,\text{GeV}$ *with the following values of* $\sin^2(\theta_W)$ : 0.21, 0.23 *and* 0.25.

Using the values for $M_Z$ and $\Gamma_Z$ from [6] and equation (1.5), the resulting forward-backward asymmetries are shown in table 1.4

| $\sqrt{s}$/GeV | $\sin^2(\theta_W)$ | | |
|---|---|---|---|
| | 0.21 | 0.23 | 0.25 |
| 89.225 | −0.094 | −0.164 | −0.195 |
| 91.225 | 0.076 | 0.022 | 0.004 |
| 93.225 | 0.231 | 0.196 | 0.190 |

Table 1.4.: Forward-backward asymmetry for different energies and Weinberg angles.

# 2 Experimental Analysis

## 2.1 Analysis of event displays

In the first part of this experiment, we will learn how to distinguish between the different decay modes of the $Z^0$ boson on the basis of a graphical analysis of events. To do so, we get four Monte Carlo generated test samples, containing 20 events of only one decay mode of the $Z^0$ each and four mixed samples, each containing 20 events recorded with the OPAL detector. To analyze the data samples, we will use the program *GROPE*, which displays the events in a 2D-overview of the detector. These can be characterized by the four quantities

- *NCharged*: The number of charged tracks measured in the detector,
- *SumP*: The sum of all the charged tracks momenta,
- *Energy ECAL*: The total energy deposited in the electromagnetic calorimeter,
- *Energy HCAL*: The total energy deposited in the hadronic calorimeter,

which are also part of the output.

### 2.1.1 Monte Carlo generated samples

We start with the four prepared data samples ('runs') of $e^-e^+$, $\mu^-\mu^+$, $\tau^-\tau^+$ and $q\bar{q}$, each containing 20 events of the respective $Z^0$ decay channel only. These have been generated with the help of *Monte Carlo simulations* and make it possible to find criteria for ascribing specific events on the display to the different decay channels. The different samples can be run by using the command 'grope x', where x $\in$ {ee, mm, tt, qq} is self-explanatory. The detectors responses, depicted with *GROPE* on the display, are shown in figure 2.1.

Writing down the values of the variables mentioned above for all samples and creating histograms for the frequencies of the values in each sample separately, we find the figures 2.2-2.5.

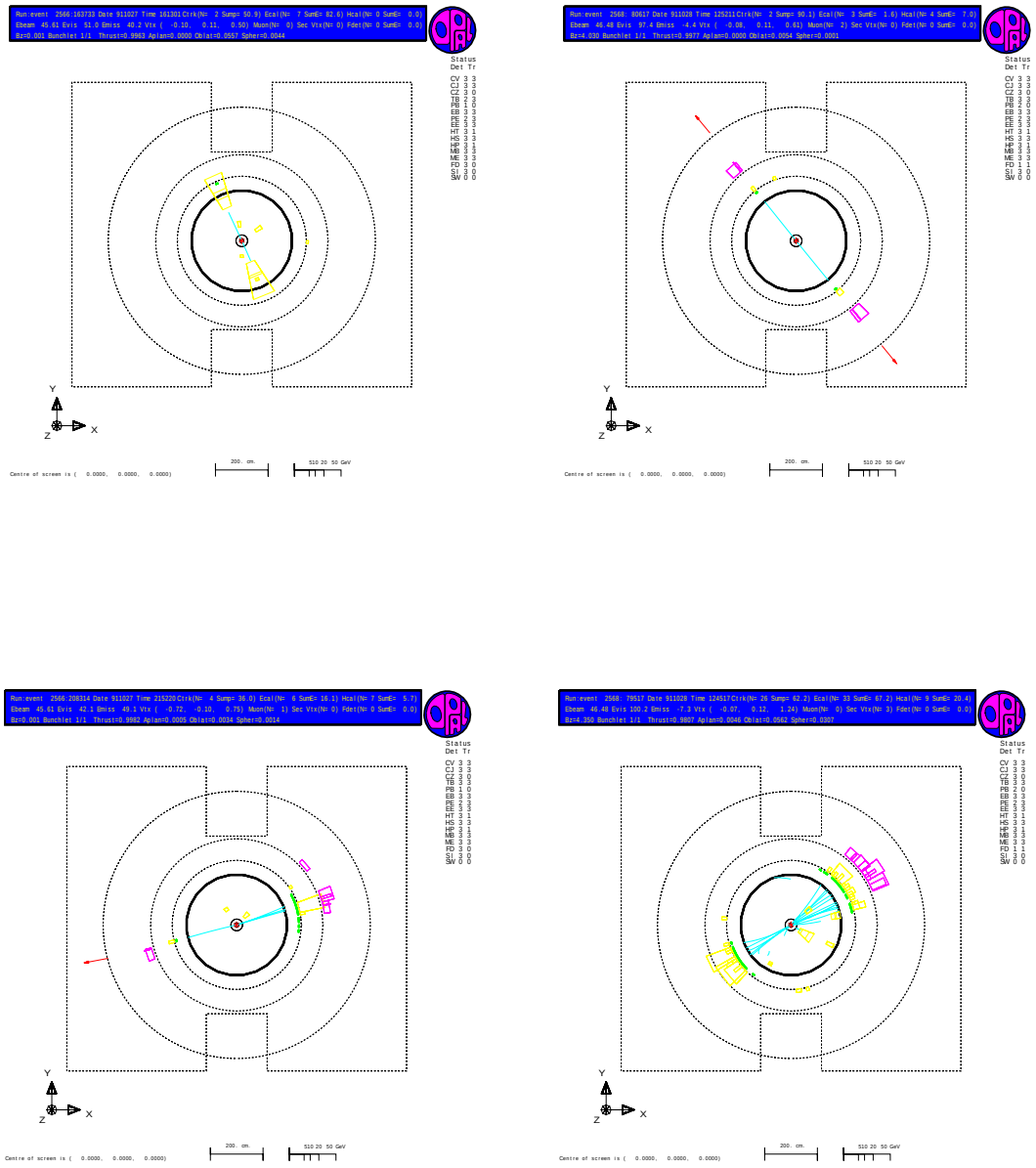

Figure 2.1.: The detectors response for a specific $e^-e^+$-, $\mu^-\mu^+$-, $\tau^-\tau^+$- and $q\bar{q}$-event (from top-left to bottom-right) as displayed by *GROPE*. The particles tracks in the inner are displayed in teal, the reaction of the electromagnetic and hadronic calorimeters in yellow and purple respectively and the reaction of the muon chamber in red.

With the help of the histograms, it is now an easy job to find cuts for an optimal separation of the different $Z^0$ decay modes. We find table 2.1, containing lower

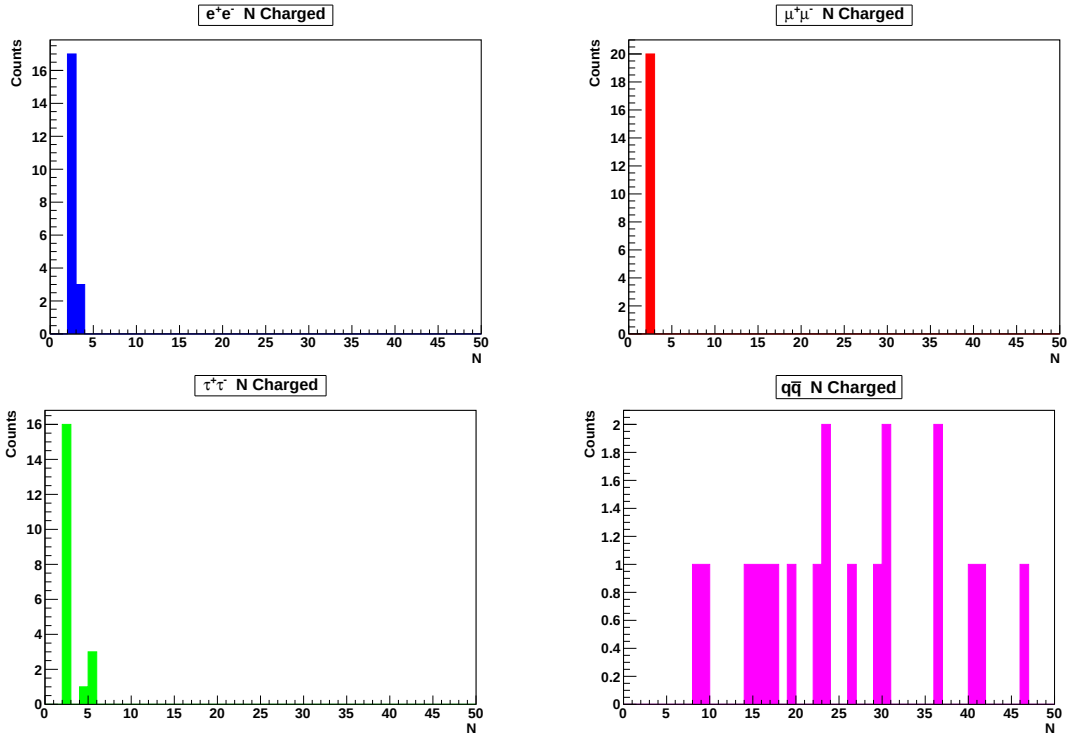


Figure 2.2.: The histograms showing the frequencies of the variable 'NCharged' for the different samples $e^-e^+$, $\mu^-\mu^+$, $\tau^-\tau^+$ and $q\bar{q}$.

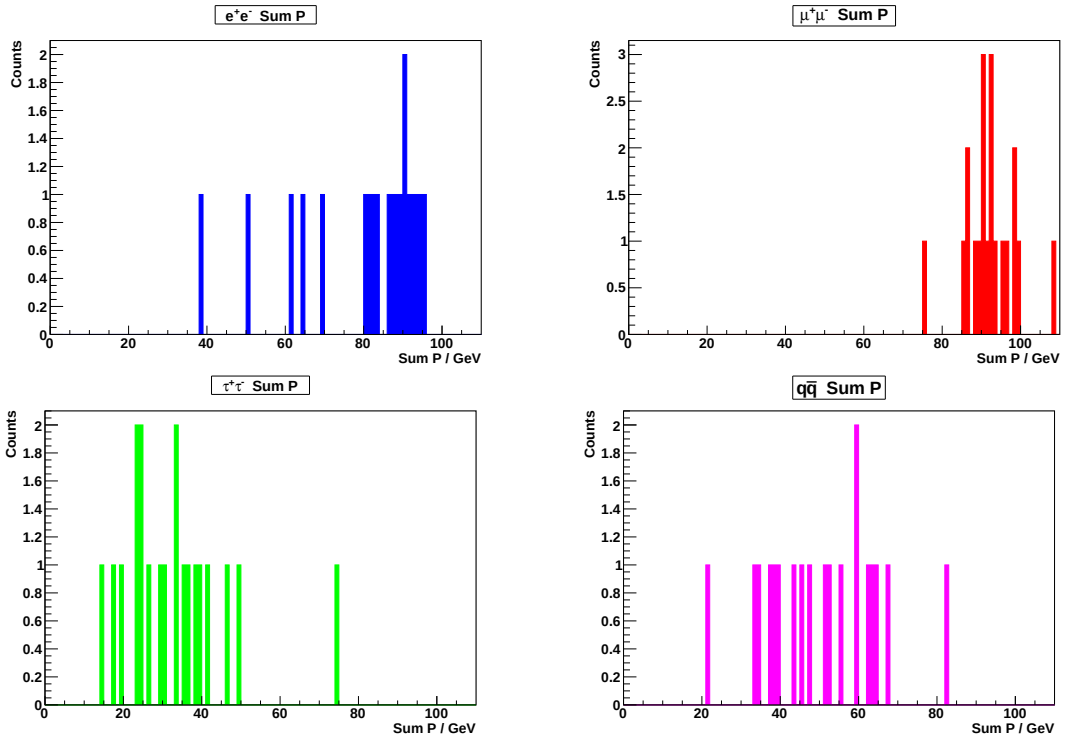


Figure 2.3.: The histograms showing the frequencies of the variable 'SumP' for the different samples $e^-e^+$, $\mu^-\mu^+$, $\tau^-\tau^+$ and $q\bar{q}$.

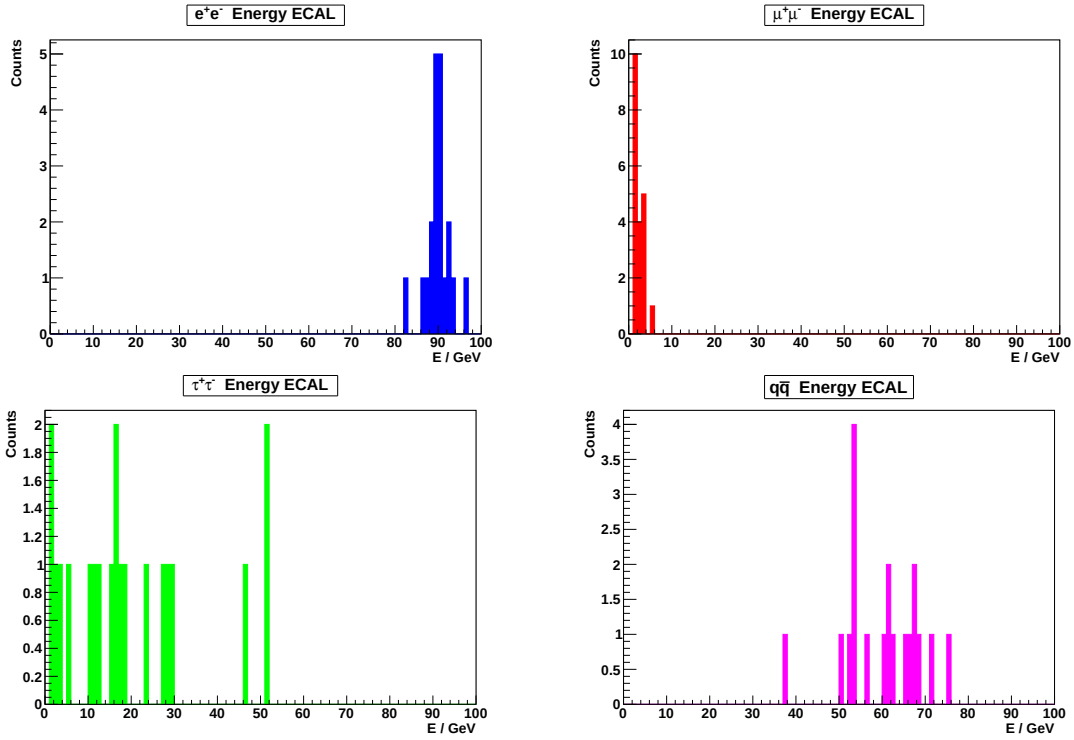


Figure 2.4.: The histograms showing the frequencies of the variable 'SumE' for the different samples $e^-e^+$, $\mu^-\mu^+$, $\tau^-\tau^+$ and $q\bar{q}$.

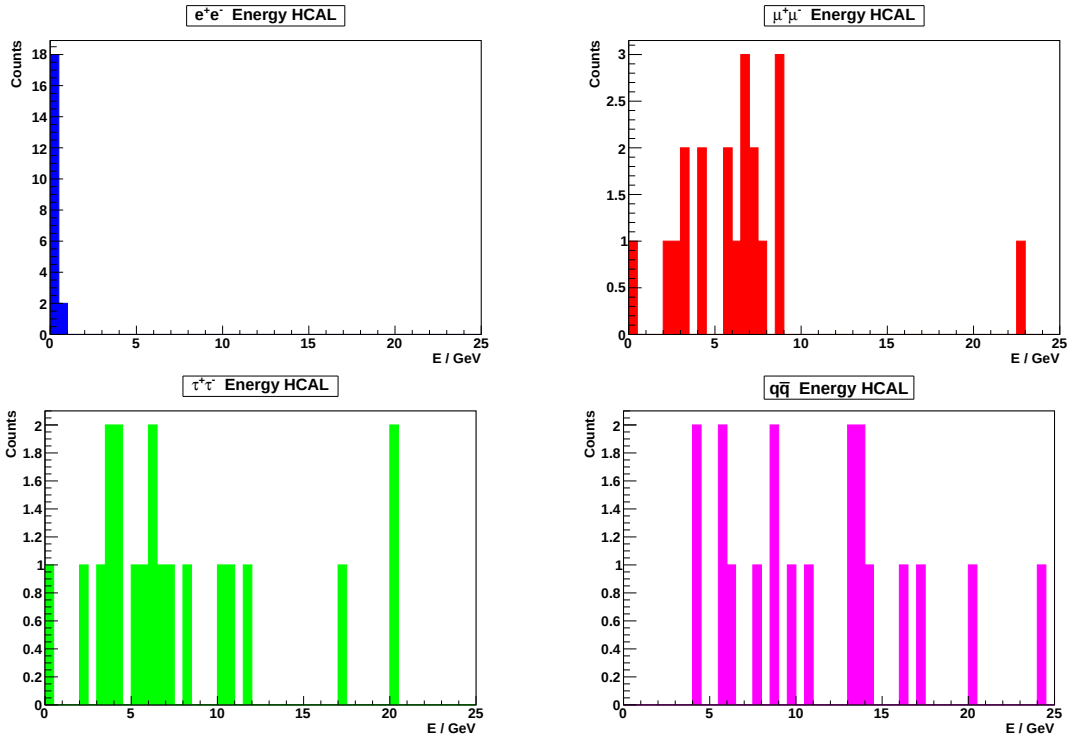


Figure 2.5.: The histograms showing the frequencies of the variable 'SumH' for the different samples $e^-e^+$, $\mu^-\mu^+$, $\tau^-\tau^+$ and $q\bar{q}$.

and upper bounds for the different variables and decay channels. An appearing '–' means that there is no cut to be applied.

| | N Charged | | Sum P | | Energy ECAL | | Energy HCAL | |
|---|---|---|---|---|---|---|---|---|
| | min | max | min | max | min | max | min | max |
| $e^-e^+$ | – | 4 | 70 | 100 | 85 | 95 | – | 1 |
| $\mu^-\mu^+$ | – | 4 | 80 | 105 | – | 5 | – | 12 |
| $\tau^-\tau^+$ | – | 8 | – | 60 | – | 40 | – | 22 |
| $q\bar{q}$ | 8 | – | – | 80 | 40 | 85 | 5 | 30 |

Table 2.1.: The cuts read off from the histograms, 'min' and 'max' refer to the lower and upper bound respectively and '–' depicts no restriction. Given the values of the variables and applying these cuts, one can identify a specific event with a certain decay channel.

In order to make the next part of the experiment more transparent, we create a decision tree with whose help one can uniquely ascribe an event to a decay channel. The decision tree, which makes use of table 2.1, is depicted in figure 2.6.

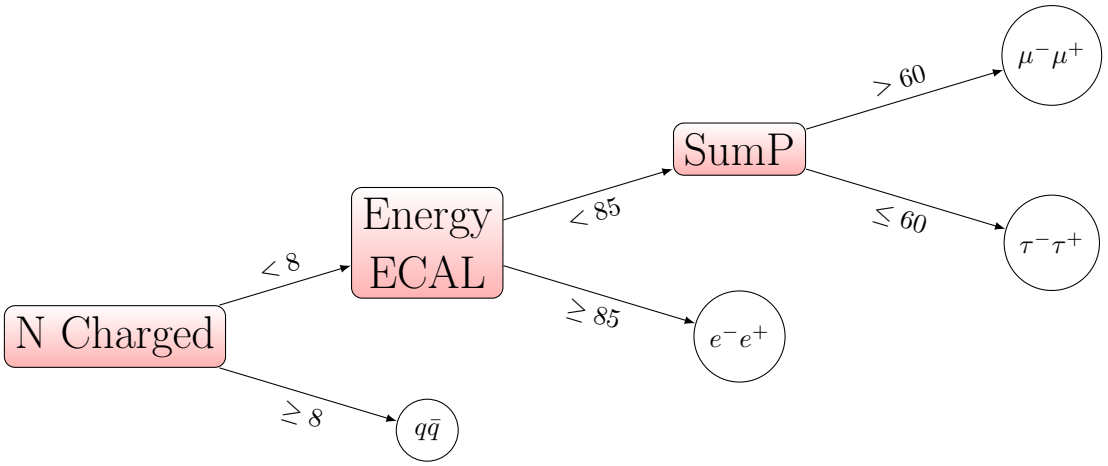


Figure 2.6.: The decision tree in order to ascribe a decay channel to an event, created using table 2.1. When in doubt, one can go back to table 2.1. (Created in TikZ).

### 2.1.2 Mixed Sample

Having learnt how to distinguish between the different decay modes, we want to use the cuts from the previous part in order to ascribe one of the four decay channels to the events of a mixed sample. Our group was assigned the sample 'test1', which can be run from the console with 'grope test1' and contains 20 'real' OPAL events.

Writing down the values of the four variables, making use of the decision tree in figure 2.6 and also a determination per graphical estimate, we obtain table 2.2.

| Event | N Ch. | Sum P | ECAL | HCAL | Dec. (tree) | Dec. (gr.) |
|---|---|---|---|---|---|---|
| 1080 | 19 | 39.5 | 44.3 | 15.6 | $q\bar{q}$ | $q\bar{q}$ |
| 2387 | 36 | 42.8 | 57.1 | 12.5 | $q\bar{q}$ | $q\bar{q}$ |
| 5386 | 2 | 95.7 | 93.4 | 0.0 | $e^-e^+$ | $e^-e^+$ |
| 6057 | 2 | 90.8 | 1.4 | 4.1 | $\mu^-\mu^+$ | $\mu^-\mu^+$ |
| 6696 | 4 | 36.5 | 35.8 | 10.8 | $\tau^-\tau^+$ | $\tau^-\tau^+$ |
| 7137 | 2 | 97.0 | 2.2 | 8.9 | $\mu^-\mu^+$ | $\mu^-\mu^+$ |
| 7219 | 68 | 42.9 | 48.5 | 6.2 | $q\bar{q}$ | $q\bar{q}$ |
| 8323 | 5 | 35.0 | 40.8 | 3.3 | $\tau^-\tau^+$ | $\tau^-\tau^+$ |
| 8641 | 21 | 75.8 | 45.8 | 21.0 | $q\bar{q}$ | $q\bar{q}$ |
| 9149 | 2 | 95.2 | 1.3 | 7.9 | $\mu^-\mu^+$ | $\mu^-\mu^+$ |
| 9289 | 2 | 22.7 | 43.4 | 0 | $\tau^-\tau^+$ | $e^-e^+$ |
| 9593 | 4 | 44.3 | 37.8 | 2.6 | $\tau^-\tau^+$ | $\tau^-\tau^+$ |
| 9880 | 21 | 53.1 | 36.2 | 22.9 | $q\bar{q}$ | $q\bar{q}$ |
| 10900 | 2 | 89.5 | 92.0 | 0.0 | $e^-e^+$ | $e^-e^+$ |
| 11844 | 2 | 89.1 | 89.7 | 0.0 | $e^-e^+$ | $e^-e^+$ |
| 13556 | 2 | 4.1 | 4.4 | 0.0 | $\tau^-\tau^+$ | $\tau^-\tau^+$ |
| 14063 | 2 | 87.8 | 1.4 | 4.3 | $\mu^-\mu^+$ | $\mu^-\mu^+$ |
| 14640 | 2 | 75.3 | 90.0 | 0 | $e^-e^+$ | $e^-e^+$ |
| 14744 | 2 | 93.7 | 1.6 | 6.8 | $\mu^-\mu^+$ | $\mu^-\mu^+$ |
| 15755 | 2 | 67.1 | 93.6 | 0.0 | $e^-e^+$ | $e^-e^+$ |

Table 2.2.: Result of the channel assignment for the different events in the sample 'test1', making use of the decision tree and a graphical estimate.

## 2.2 Statistical Analysis of $Z^0$ decays

In order to measure the mass and decay width of the $Z^0$, as well as the number of generations of light neutrinos and the Weinberg angle in the second part of this experiment, we need a large number of events as a reference. This makes a graphical analysis inconvenient, such that we will analyze the events on a statistical basis only now. This will be done with the program *PAW*, where additionally to the variables *NCharged*, *PCharged* (former *SumP*), *E_ECal* and *E_HCal* for each event, we now have the total beam energy $\sqrt{s}/2$ denoted by *E_LEP*, the angle $\cos\theta$ between incoming $e^+$ and outgoing $\bar{f}$, and the angle $\cos\alpha$ between the beam and thrust axis. These are all stored in an array-like structure called *ntuple*.

Like in the previous part of the experiment, we have simulated Monte Carlo events and events recorded with the OPAL detector. Analyzing the Monte Carlo generated events first, we optimize our cuts from the first part of the experiment and have to find a cut which separates the s-channel from the t-channel for the $e^-e^+$-sample. We then use these test samples – remember, each contains simulated events of one channel only – to find a to be defined efficiency matrix, telling us how many events of the underlying set have been identified as such after applying the cuts. This way, we also take care of background effects. With the help of this efficiency matrix, we can give a good approximation of the 'real' values, based on the 'ascribed' ones for the data samples recorded with the OPAL detector. We calculate the differential cross section for the leptonic and hadronic channels and determine the forward-backward asymmetry from the muon final states.

*PAW* accepts Fortran and C syntax. As an example, one can plot the *PCharged* distribution of the electron test sample for the events with more than two charged tracks by writing

```
n/plot electrons.pcharged ncharged > 2
```

in the shell script.

### 2.2.1 Monte Carlo generated samples and the efficiency matrix

We now redefine our cuts from table 2.1 to the values given in table 2.3, by analyzing the large amount of events from Monte Carlo generated samples on a statistical basis. We fix a cut for $SumP \in [0, 120]$ for all samples, as particles with zero energy are unphysical, while the upper bound respects the limited energy of the detector. For the electron decay channel, we additionally have to separate the s-channel from the t-channel contribution, because the other decays only exist in the s-channel. As

the t-channel dominates for small angles, while the s-channel dominates for large angles, we set a cut on the angle between the initial and final state particles for the $e^-e^+$-sample:

$$\cos\theta \in [-0.9, 0.5].$$

If no additional bound (i.e. a '$-$') is given in table 2.3, the general cut on $SumP$ from above still holds true. The corresponding figures C.1-C.4 can be found in the appendix.

| | N Charged | | Sum P | | Energy ECAL | | Energy HCAL | |
|---|---|---|---|---|---|---|---|---|
| | min | max | min | max | min | max | min | max |
| $e^-e^+$ | – | 3 | 50 | – | 80 | 100 | – | 2 |
| $\mu^-\mu^+$ | – | 3 | 75 | – | – | 6 | – | 15 |
| $\tau^-\tau^+$ | – | 6 | – | 60 | – | 70 | – | 20 |
| $q\bar{q}$ | 7 | – | – | 80 | 30 | 80 | 2 | 50 |

Table 2.3.: The redefined cuts for the large data samples. Otherwise, the table has the same content as table 2.1.

For later convenience and in order to give meaning to the matrix notation of the efficiencies, we introduce a vector notation

$$N = \begin{pmatrix} \#e \\ \#\mu \\ \#\tau \\ \#q \end{pmatrix},$$

denoting the numbers of total/ascribed $e^-e^+$-, $\mu^-\mu^+$-, $\tau^-\tau^+$- and $q\bar{q}$-events in the different samples before/after applying the cuts. Multiplying such a vector to the – to be defined – matrix, we will be able to get the real number of events depending on the ascribed ones.

For the total number of events in this notation, we look at the samples with only a cut applied to the $e^-e^+$-sample, separating the s-channel from the t-channel and

find

$$\tilde{N}_{\text{tot}} = \begin{pmatrix} 20531 \\ 94381 \\ 79214 \\ 98563 \end{pmatrix}.$$

Using the cut to get rid of the t-channel contribution of the cross section for the $e^-e^+$ final states also removes part of the s-channel. Remembering that the s-channel differential cross section behaves like $(1+\cos^2\theta)$ and that we cut $\cos\theta \in [-0.9, 0.5]$, we can take this into account by multiplying the $\tilde{N}^1_{\text{tot}}$-entry with the correction factor

$$C = \frac{\int_{-1}^{1} 1+\cos^2\theta \,\mathrm{d}\cos\theta}{\int_{-0.9}^{0.5} 1+\cos^2\theta \,\mathrm{d}\cos\theta} = 1.5829.$$

We then arrive at

$$N_{\text{tot}} = \begin{pmatrix} 32499 \\ 94381 \\ 79214 \\ 98563 \end{pmatrix}, \tag{2.1}$$

where we rounded to integer numbers because it does not make sense to talk about non-integer particle numbers.

Additionally, we now introduce said matrix notation, writing the used samples in different columns and the applied cuts in different rows. The value in the specific entry $(i, j)$ then denotes the remaining events of the sample $j$ upon applying the cuts $i$. For our cuts, this gives

$$n = \begin{array}{c} \text{Cuts} \downarrow \backslash \text{Sample} \rightarrow \\ e \\ \mu \\ \tau \\ q \end{array} \begin{array}{c} \begin{array}{cccc} e & \mu & \tau & q \end{array} \\ \begin{pmatrix} 18254 & 0 & 9 & 0 \\ 0 & 74796 & 13 & 0 \\ 246 & 1451 & 66807 & 243 \\ 0 & 0 & 526 & 89618 \end{pmatrix} \end{array}.$$

Calculating what part of the underlying set is left after applying the cuts, we divide

the columns by the corresponding value $N_{\text{tot}}^j$ of the vector (2.1), i.e.

$$\varepsilon_{ij} = \frac{n_{ij}}{N_{\text{tot}}^j}. \tag{2.2}$$

This results in

$$\varepsilon = \begin{pmatrix} 0.56169 & 0 & 0.00011 & 0 \\ 0 & 0.79249 & 0.00016 & 0 \\ 0.00757 & 0.01537 & 0.84337 & 0.00247 \\ 0 & 0 & 0.00664 & 0.90925 \end{pmatrix}, \tag{2.3}$$

where we rounded to five decimal places and from now on drop the additional legend for the rows and columns.

Considering eq. (2.2), one notices that the numerator and denominator on the right-hand side are correlated because a change in $N_{\text{tot}}$ also results in a change of $n$. For the errors on these values, one thus has to assume a binomial distribution. Following appendix B, we can use eq. (B.1) to calculate this binomial distributed error. To this end, we calculate $\sqrt{\epsilon_{ij}(1-\epsilon_{ij})}$ for each entry of the matrix (2.3) and divide every column by the square root of the respective entry of the vector (2.1). In other words, we have

$$\Delta\varepsilon_{ij} = \sqrt{\frac{\varepsilon_{ij}(1-\varepsilon_{ij})}{N_{\text{tot}}^j}}$$

and – again rounding to five decimal places – get the matrix

$$\Delta\varepsilon = \begin{pmatrix} 0.00275 & 0 & 0.00004 & 0 \\ 0 & 0.00132 & 0.00005 & 0 \\ 0.00048 & 0.00040 & 0.00129 & 0.00016 \\ 0 & 0 & 0.00029 & 0.00091 \end{pmatrix}. \tag{2.4}$$

If we further normalize $N_{\text{tot}}$ of eq. (2.1) to

$$\hat{N}_{\text{total}} = \begin{pmatrix} 100000 \\ 100000 \\ 100000 \\ 100000 \end{pmatrix},$$

we have to multiply each column of the matrix (2.3) and (2.4) with 100000. As we will not use this result in the future, this calculation is left to the reader.

What we have obtained now, is a matrix that gives the number of ascribed $e^-e^+$-, $\mu^-\mu^+$-, $\tau^-\tau^+$- and $q\bar{q}$-events in terms of the underlying set of total events in the samples, i.e.

$$N_{\text{asc}} = \varepsilon N_{\text{tot}}.$$

What we later need, is the inverse of this equation. We will have a number of registered events after applying the cuts and want the real number of events in the sample, i.e.

$$N_{\text{tot}} = \varepsilon^{-1} N_{\text{asc}}. \tag{2.5}$$

We thus invert the matrix (2.3) with *Mathematica* using the method *'CofactorExpansion*. To invert the errors, we make use of eq. (B.2) in appendix B:

$$\Delta(\varepsilon^{-1}) = \left|(\varepsilon^{-1})(\Delta\varepsilon)(\varepsilon^{-1})\right| \tag{2.6}$$

and eventually find

$$\varepsilon^{-1} = \begin{pmatrix} 178035.00 & 0.47 & -23.99 & 0.07 \\ 0.33 & 1.26 & -24.56 & 0.07 \\ -1598.00 & -2300.28 & 118575.00 & -321.52 \\ 11.67 & 16.80 & -865.95 & 109984.00 \end{pmatrix} \times 10^{-5}, \tag{2.7}$$

as well as

$$\Delta(\varepsilon^{-1}) = \begin{pmatrix} 872.28 & 0.16 & 17.90 & 0.06 \\ 0.07 & 210.04 & 6.73 & 0.02 \\ 57.80 & 52.58 & 181.09 & 19.79 \\ 0.74 & 1.10 & 35.44 & 110.43 \end{pmatrix} \times 10^{-5}. \tag{2.8}$$

Here, we changed to the scientific notation because of the small values that appear in the inverse matrix.

### 2.2.2 OPAL data and the total cross section

In this part, we work with a data sample recorded with the OPAL detector. There are events of the different types, $e^-e^+$, $\mu^-\mu^+$, $\tau^-\tau^+$ and $q\bar{q}$, taken at seven different centre-of-mass energies in this sample. For each of these energies, we use the cuts

found in the previous part to determine the events in the hadronic and leptonic channels. What we find is depicted in table 2.4, where the errors on the entries follow a poisson distribution and are thus given by the square root of the respective value – again, rounded to integer values. We were assigned the sample *'data 1'*.

| $\sqrt{s}$/GeV | Cuts | | | |
|---|---|---|---|---|
| | $e^-e^+$ | $\mu^-\mu^+$ | $\tau^-\tau^+$ | $q\bar{q}$ |
| 88.47 | $113 \pm 11$ | $114 \pm 11$ | $156 \pm 12$ | $3153 \pm 56$ |
| 89.46 | $172 \pm 13$ | $199 \pm 14$ | $207 \pm 14$ | $4666 \pm 68$ |
| 90.22 | $203 \pm 14$ | $291 \pm 17$ | $254 \pm 16$ | $6686 \pm 82$ |
| 91.22 | $2074 \pm 46$ | $3287 \pm 57$ | $3373 \pm 58$ | $79943 \pm 283$ |
| 91.97 | $304 \pm 17$ | $559 \pm 24$ | $554 \pm 24$ | $13045 \pm 114$ |
| 92.96 | $122 \pm 11$ | $227 \pm 15$ | $263 \pm 16$ | $5871 \pm 77$ |
| 93.71 | $155 \pm 12$ | $275 \pm 17$ | $277 \pm 17$ | $6491 \pm 81$ |

Table 2.4.: The determined number of events in the hadronic and leptonic channels after applying the cuts onto the OPAL sample 'data 1' at the seven different centre-of-mass energies.

As discussed in section 2.2.1, we have to use eq. (2.5) in order to get the real number of hadronic and leptonic events as a function of the ascribed events given in table 2.4. In other words, we have to multiply the rows of table 2.4 with the inverse efficiency matrix (2.7) to get the real number of events. The error on these values is simply given by gaussian error propagation, where one has to make use of eq. (2.6) again. What we find is shown in table 2.5, where – once again – we rounded to integer numbers.

| $\sqrt{s}$/GeV | $N^e_{\text{real}}$ | $N^\mu_{\text{real}}$ | $N^\tau_{\text{real}}$ | $N^q_{\text{real}}$ |
|---|---|---|---|---|
| 88.48021 | $201 \pm 19$ | $144 \pm 13$ | $170 \pm 14$ | $3466 \pm 62$ |
| 89.47158 | $306 \pm 23$ | $251 \pm 18$ | $223 \pm 16$ | $5130 \pm 75$ |
| 90.22720 | $361 \pm 25$ | $367 \pm 22$ | $270 \pm 18$ | $7351 \pm 90$ |
| 91.23223 | $3692 \pm 83$ | $4147 \pm 73$ | $3634 \pm 71$ | $87896 \pm 323$ |
| 91.97109 | $541 \pm 31$ | $705 \pm 30$ | $597 \pm 27$ | $14343 \pm 126$ |
| 92.97091 | $217 \pm 20$ | $286 \pm 19$ | $286 \pm 19$ | $6455 \pm 84$ |
| 93.71841 | $276 \pm 22$ | $347 \pm 21$ | $299 \pm 19$ | $7137 \pm 89$ |

Table 2.5.: The 'real' number of events in the hadronic and leptonic channels, i.e. the values from table 2.4 corrected for the efficiency and subtracted by the background.

Given the integrated luminosities for the different centre-of-mass energies taken

from [7] and depicted in table 2.6, we use eq. (1.7) to find the cross sections.

| $\sqrt{s}$/GeV | $\mathcal{L}\,\mathrm{d}t/\mathrm{nb}^{-1}$ |
|---|---|
| 88.48021 | $675.8590 \pm 5.721257$ |
| 89.47158 | $543.6270 \pm 4.830643$ |
| 90.22720 | $419.7760 \pm 3.974844$ |
| 91.23223 | $3122.204 \pm 22.31760$ |
| 91.97109 | $639.8380 \pm 5.577354$ |
| 92.97091 | $479.2400 \pm 4.481870$ |
| 93.71841 | $766.8380 \pm 6.497519$ |

Table 2.6.: The integrated luminosities including their errors for the centre-of-mass energies used in the sample 'data 1'. Taken from [7].

The resulting cross sections have to be corrected with table 2.7, due to radiative corrections from higher order Feynman diagrams. The result is given in table 2.8.

| $\sqrt{s}$/GeV | hadronic correction/nb | leptonic correction/nb |
|---|---|---|
| 88.47 | 2.0 | 0.09 |
| 89.46 | 4.3 | 0.20 |
| 90.22 | 7.7 | 0.36 |
| 91.22 | 10.8 | 0.52 |
| 91.97 | 4.7 | 0.22 |
| 92.96 | −0.2 | −0.01 |
| 93.71 | −1.6 | −0.08 |

Table 2.7.: Radiative corrections for the cross sections at seven centre-of-mass energies in the region of the samples energies. Taken from [2].

### 2.2.3 The forward-backward Asymmetry

In this part, we want to determine the forward-backward asymmetry from the OPAL data in order to calculate the *Weinberg angle* $\sin^2\theta$. For this purpose, we investigate the muon final states and measure the number of muons flying in forward $(0^\circ - 180^\circ)$ and backward $(180^\circ - 360^\circ)$ direction respectively. The error on this number is poisson distributed like in the previous part for table 2.4 and thus given by the square root of the value. The result is shown in table 2.9.

Having obtained these values, we can define

$$A_{\mathrm{FB}} = \frac{N_f - N_b}{N_f + N_b}, \tag{2.9}$$

| $\sqrt{s}$/GeV | $\sigma^e$/nb | $\sigma^\mu$/nb | $\sigma^\tau$/nb | $\sigma^q$/nb |
|---|---|---|---|---|
| 88.48021 | $0.39 \pm 0.03$ | $0.30 \pm 0.02$ | $0.34 \pm 0.02$ | $7.1 \pm 0.1$ |
| 89.47158 | $0.76 \pm 0.04$ | $0.66 \pm 0.03$ | $0.61 \pm 0.03$ | $13.7 \pm 0.2$ |
| 90.22720 | $1.22 \pm 0.06$ | $1.23 \pm 0.05$ | $1.00 \pm 0.04$ | $25.2 \pm 0.3$ |
| 91.23223 | $1.70 \pm 0.03$ | $1.85 \pm 0.03$ | $1.68 \pm 0.02$ | $39.0 \pm 0.2$ |
| 91.97109 | $1.07 \pm 0.05$ | $1.32 \pm 0.05$ | $1.15 \pm 0.04$ | $27.1 \pm 0.3$ |
| 92.97091 | $0.44 \pm 0.04$ | $0.59 \pm 0.04$ | $0.41 \pm 0.04$ | $13.3 \pm 0.2$ |
| 93.71841 | $0.28 \pm 0.03$ | $0.37 \pm 0.03$ | $0.31 \pm 0.02$ | $7.7 \pm 0.1$ |

Table 2.8.: The cross sections for the four different decay channels at the seven given centre-of-mass energies.

| $\sqrt{s}$/GeV | $N_{f,\cos([0,1])}$ | $N_{b,\cos([-1,0])}$ |
|---|---|---|
| 88.47 | $46 \pm 7$ | $68 \pm 8$ |
| 89.46 | $102 \pm 10$ | $97 \pm 10$ |
| 90.22 | $129 \pm 11$ | $162 \pm 13$ |
| 91.22 | $1624 \pm 40$ | $1663 \pm 41$ |
| 91.97 | $285 \pm 17$ | $274 \pm 17$ |
| 92.96 | $136 \pm 12$ | $91 \pm 10$ |
| 93.71 | $154 \pm 12$ | $121 \pm 11$ |

Table 2.9.: The number of muon final states in forward and backward direction including their poisson distributed errors for the seven different centre-of-mass energies.

analogously to eq. (1.5). Here, $N_f$ and $N_b$ denote the number of muons flying in forward and backward direction respectively. Because of higher order effects, we have to consider radiative corrections and correct the values with the help of table 2.10. What we then find is depicted in table 2.11, where the error on $A_{\mathrm{FB}}$ follows a binomial distribution, because the numerator and denominator are not independent.

We know that for energies close to the peak, eq. (1.6) holds true. According to table 2.9, 91.23223 GeV is the closest one to the peak out of the seven centre-of-mass energies. We can then solve eq. (1.6) to find the *Weinberg angle*:

$$\sin^2\theta_W \approx \frac{1}{4}\left(1 - \sqrt{\frac{A_{\mathrm{FB}}^{\mathrm{peak}}}{3}}\right) = 0.23842 \pm 0.00125.$$

This value is close to the $5\sigma$ confidence level of the literature value from [6], being

$$\sin^2\theta_W^{\mathrm{lit}} = 0.23122 \pm 0.00015.$$

| $\sqrt{s}$/GeV | Radiative correction |
|---|---|
| 88.47 | 0.021512 |
| 89.46 | 0.019262 |
| 90.22 | 0.016713 |
| 91.22 | 0.018293 |
| 91.97 | 0.030286 |
| 92.96 | 0.062196 |
| 93.71 | 0.093850 |

Table 2.10.: Radiative corrections for $A_{\mathrm{FB}}$ for seven different centre-of-mass energies in the region of the centre-of-mass energies of the six available samples. Taken from [2].

| $\sqrt{s}$/GeV | $A_{\mathrm{FB}}$ |
|---|---|
| 88.48021 | $-0.1714705 \pm 0.0419767$ |
| 89.47158 | $0.0443876 \pm 0.0145997$ |
| 90.22720 | $-0.0966891 \pm 0.0190890$ |
| 91.23223 | $0.0064281 \pm 0.0013939$ |
| 91.97109 | $0.0499640 \pm 0.0092149$ |
| 92.97091 | $0.2604339 \pm 0.0291289$ |
| 93.71841 | $0.2138500 \pm 0.0247253$ |

Table 2.11.: The forward-backward asymmetry, determined with eq. (2.9) from the values in table 2.9 and corrected by table 2.10.

A possible reason for our result being so far away from the literature value is of course that we took the peak to be at an energy of 91.23223 GeV, a fitted curve could improve this result immensely.

### 2.2.4 Lepton Universality

From the standard models point of view, the $Z^0$ boson should couple identical to the three charged leptons and thus the cross section for each final state $l^- l^+$ (at the peak) is expected to be the same. This is referred to as *lepton universality* in this context. Using eq. (1.3), which is valid at the peak $\sqrt{s} = M_{Z^0}$, we find with the literature values from [6] that

$$\sigma_l^{\mathrm{peak}} = (1.9982 \pm 0.0051)\,\mathrm{nb}. \tag{2.10}$$

Note the difference to table 1.2, where we used the values from [2].

Using table 2.8 to extract the cross sections at the centre-of-mass energy closest to $M_{Z^0}$ being $\sqrt{s} = 91.23223$, we find

$$\begin{aligned} \sigma^e_{\text{peak}} &= (1.70 \pm 0.03)\,\text{nb}, \\ \sigma^\mu_{\text{peak}} &= (1.85 \pm 0.03)\,\text{nb}, \\ \sigma^\tau_{\text{peak}} &= (1.68 \pm 0.02)\,\text{nb}. \end{aligned} \tag{2.11}$$

While the values for the electron and tauon agree with each other within a $1\sigma$ confidence level, they do not agree with the expected value of eq. (2.10). The value for the muon is the closest one to eq. (2.10) – even though without lying within a $5\sigma$ confidence level – but it does not agree with the other values from eq. (2.11). A possible cause for the wrong electron value could be the removal of the t-channel and adding of the partly removed s-channel. Yet, at first sight, the disagreeing values for the muon and tauon seem inexplicable if we assume that our efficiency matrix (2.7) is correct.

As an additional test, we now want to calculate the ratios of the hadronic to the leptonic total cross sections at the peak,

$$\frac{\sigma^q_{\text{peak}}}{\sigma^l_{\text{peak}}} \quad \text{for} \quad l = e, \mu, \tau,$$

and compare these to the literature value, corresponding to the ratio of the partial decay widths $\Gamma_q/\Gamma_l$. This ratio can be found in [6] and is depicted in table 2.12, together with the ratios of the hadronic and leptonic cross sections.

| | $e^-e^+$ | $\mu^-\mu^+$ | $\tau^-\tau^+$ | $\Gamma_q/\Gamma_l$ |
|---|---|---|---|---|
| $\sigma^q_{\text{peak}}/\sigma^l_{\text{peak}}$ | $22.94 \pm 0.42$ | $21.08 \pm 0.36$ | $23.21 \pm 0.30$ | $20.767 \pm 0.025$ |

Table 2.12.: The ratios of the total hadronic to the leptonic cross sections at the peak and the ratio of the partial decay width $\Gamma_q$ to $\Gamma_l$.

Like for the cross sections at the peak in eq. (2.11), the value for the muon agrees the best, lying within a $1\sigma$ confidence level. The value for the electron and tauon do not agree with this value and the only reasonable argument for this can be that our efficiency matrix (2.7) is not a good ansatz. The tauon and hadron channel have a large overlap, such that analyzing table 2.12, we note that some of the tau final states could have been identified wrongly, particularly as hadron final states.

### 2.2.5 Breit-Wigner fit of the cross sections

In this further part, we want to pick up where we left off in section 2.2.2, in order to obtain more information out of the found cross sections, such as the mass and width of the $Z^0$ boson. Returning to table 2.8 in section 2.2.2, we now want to plot the values of the cross sections for the different final states $e^-e^+$, $\mu^-\mu^+$, $\tau^-\tau^+$ and $q\bar{q}$ at the seven given energies. We then fit a Breit-Wigner curve to these values with help of the program *root*. The result with the corresponding parameters of the fit is shown in figures 2.7-2.10.

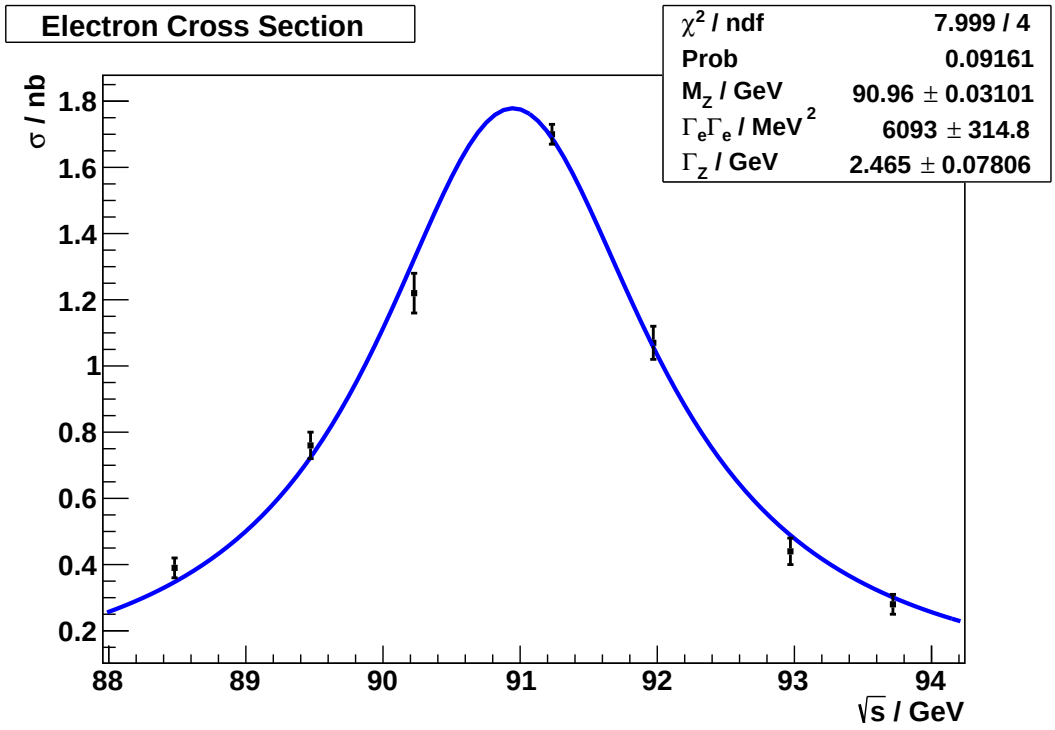


Figure 2.7.: The plotted cross section for $e^-e^+$ from table 2.8 with the corresponding fitted Breit-Wigner curve.

Collecting all these parameters in an overview and rounding the values appropriately, we find table 2.13. Determining the mass and decay width of the $Z^0$ boson out of this parameters is an easy job now. We want to use the weighted mean for this (see eq. (B.3) and eq. (B.4) in appendix B) and find

$$M_{Z^0} = (91.15 \pm 0.01)\,\text{GeV}$$
$$\Gamma_{Z^0} = (2.52 \pm 0.02)\,\text{GeV},$$

which lie within a $4\sigma$ and $2\sigma$ confidence level of the literature values from [6] re-

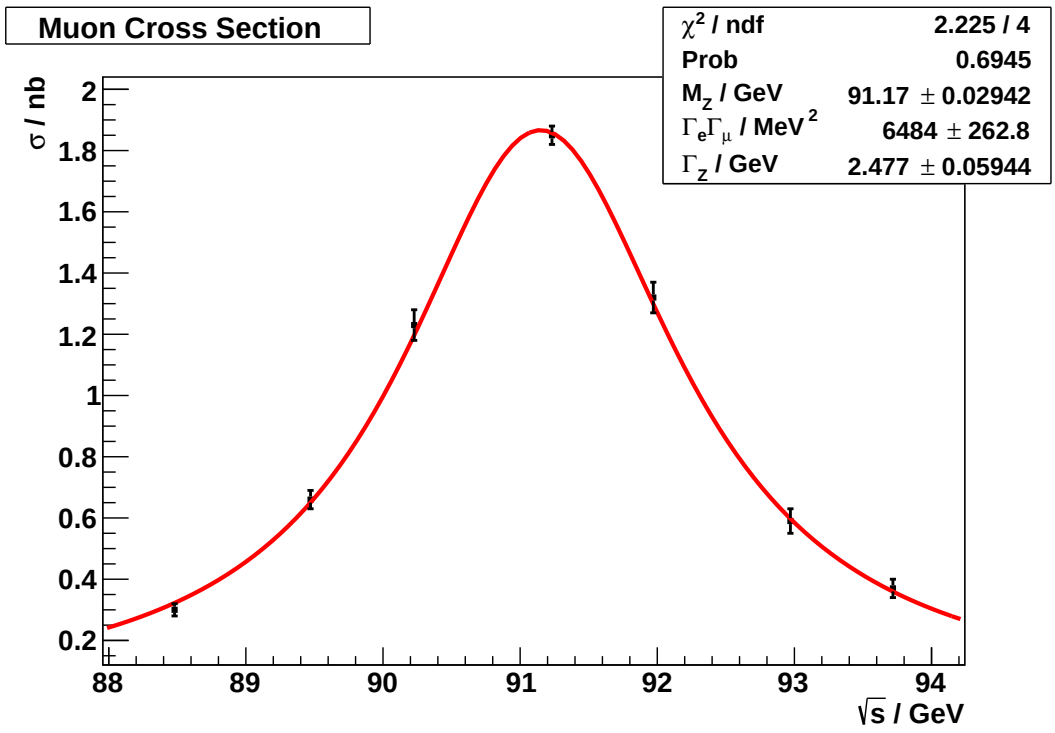


Figure 2.8.: The plotted cross section for $\mu^-\mu^+$ from table 2.8 with the corresponding fitted Breit-Wigner curve.

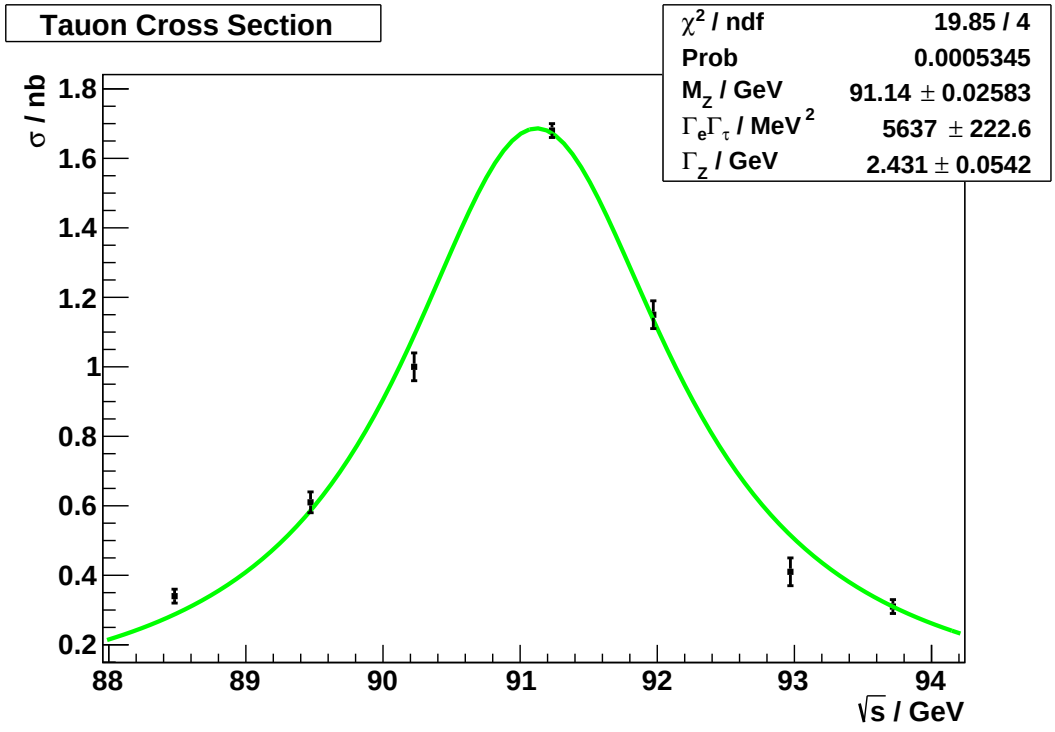


Figure 2.9.: The plotted cross section for $\tau^-\tau^+$ from table 2.8 with the corresponding fitted Breit-Wigner curve.

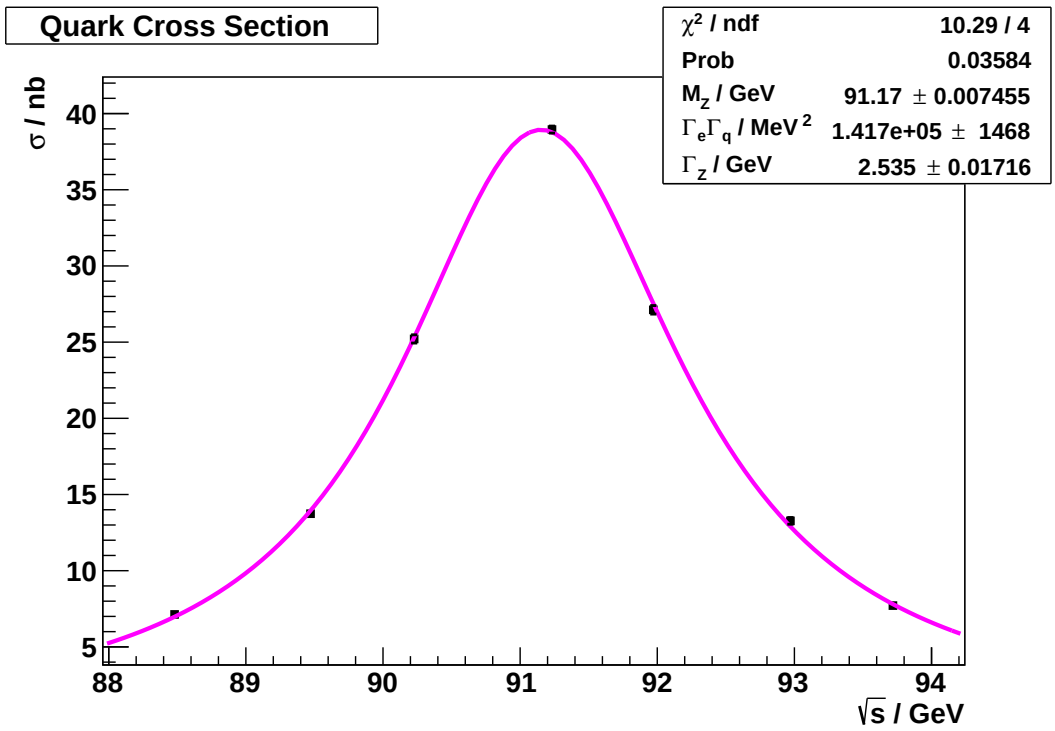


Figure 2.10.: The plotted cross section for $q\bar{q}$ from table 2.8 with the corresponding fitted Breit-Wigner curve.

| | $e^-e^+$ | $\mu^-\mu^+$ | $\tau^-\tau^+$ | $q\bar{q}$ |
|---|---|---|---|---|
| $\chi^2$/ndf | 7.999/4 | 2.225/4 | 19.85/4 | 10.29/4 |
| Prob | 0.009161 | 0.6945 | 0.0005345 | 0.03584 |
| $M_{Z^0}$/GeV | $90.96 \pm 0.03$ | $91.17 \pm 0.03$ | $91.14 \pm 0.03$ | $91.17 \pm 0.01$ |
| $\Gamma_e\Gamma_f$/MeV$^2$ | $6093 \pm 315$ | $6484 \pm 263$ | $5637 \pm 223$ | $141700 \pm 1468$ |
| $\Gamma_{Z^0}$/GeV | $2.465 \pm 0.078$ | $2.477 \pm 0.059$ | $2.431 \pm 0.054$ | $2.535 \pm 0.017$ |

Table 2.13.: The parameters of the fitted Breit-Wigner curves to the cross sections for the $Z^0$ decay into final states $e^-e^+$, $\mu^-\mu^+$, $\tau^-\tau^+$ and $q\bar{q}$.

spectively, being

$$M_{Z^0}^{\text{lit}} = (91.1876 \pm 0.0021)\,\text{GeV}$$
$$\Gamma_{Z^0}^{\text{lit}} = (2.4952 \pm 0.0023)\,\text{GeV}.$$

To calculate the partial widths $\Gamma_f$ for the different channels, we start with $\Gamma_e$, because this appears as $\Gamma_e\Gamma_e$ in the fitted parameters and is thus given by taking the square root. The remaining partial widths can then be obtained by simply

dividing $\Gamma_e$ out of $\Gamma_e\Gamma_f$. We arrive at

$$\begin{aligned}\Gamma_e &= (78.058 \pm 2.018)\,\text{MeV}\\ \Gamma_\mu &= (83.128 \pm 3.978)\,\text{MeV}\\ \Gamma_\tau &= (72.269 \pm 3.407)\,\text{MeV}\\ \Gamma_q &= (1816.670 \pm 50.395)\,\text{MeV}\end{aligned} \tag{2.12}$$

and compare these to the literature values from [6], given by

$$\begin{aligned}\Gamma_e^{\text{lit}} &= (83.91 \pm 0.12)\,\text{MeV}\\ \Gamma_\mu^{\text{lit}} &= (83.99 \pm 0.18)\,\text{MeV}\\ \Gamma_\tau^{\text{lit}} &= (84.08 \pm 0.22)\,\text{MeV}\\ \Gamma_q^{\text{lit}} &= (1744.4 \pm 2.0)\,\text{MeV}.\end{aligned}$$

The only partial decay width that agrees with the literature value within a $1\sigma$ confidence level is $\Gamma_\mu$. For the other partial decay widths, we find that $\Gamma_e$ lies within a $3\sigma$, $\Gamma_\tau$ within a $4\sigma$ and $\Gamma_q$ within a $2\sigma$ confidence level of the respective literature value.

Another obtainable feature from the fitted curves to the cross sections is the number of neutrino generations. To this end, we note that

$$\Gamma_{Z^0} = \Gamma_e + \Gamma_\mu + \Gamma_\tau + \Gamma_q + n \cdot \Gamma_\nu,$$

which can be solved for $n$, the number of neutrino generations. Inserting the obtained partial decay widths from eq. (2.12) and the theoretical prediction for $\Gamma_\nu$ from [2], we find that

$$n = 2.786 \pm 0.313.$$

Within a confidence level of $1\sigma$, this agrees with the known three neutrino generations of the standard model.

# 3 Conclusion

On the first day of the experiment, we developed a procedure in order to assign events on a statistical basis instead of a graphical analysis. This procedure seemed to do well on first sight.

The second day was aimed at calculating different properties of the $Z^0$ boson, the Weinberg angle and the number of light neutrino generations. The Weinberg angle was determined by measuring the forward-backward asymmetry of the muon channel at the center-of-mass energy closest to the $Z^0$ mass, yielding $\sin^2\theta_W = (0.23842 \pm 0.00125)$ which is out of the $5\sigma$ confidence level of the literature value. The only possible reason for this bad value seems to be our calculated (inverse) efficiency matrix and consequential wrongly assigned events. Calculating the ratio of the leptonic cross sections to the hadronic cross section, we investigated lepton universality and found a more or less unsatisfying result. The total cross sections at the $Z^0$-peak were all smaller than the expected theoretical value. While the ratio of the cross sections for the muon is still in the $1\sigma$ confidential level of the corresponding literature value, the others deviate strongly. Again, we find the (inverse) efficiency matrix as the reason. Especially the tauon cut seems to be chosen badly, as can be seen from the matrix itself, as well as the applied t-channel cut for the electrons.

Using a Breit-Wigner fitted curve for the cross sections, we found the averaged $Z^0$ mass $M_{Z^0} = (91.15 \pm 0.01)\,\text{Gev}$ and decay width $\Gamma_{Z^0} = (2.52 \pm 0.02)\,\text{GeV}$, which match with the literature values in a $4\sigma$ and $2\sigma$ confidence level respectively. Within a $1\sigma$ confidence level – though a high error – we were also able to determine the number of neutrino generations to be three, by looking at the total decay width of the $Z^0$ and the partial decay widths into the different leptons, hadrons and 'invisible' channels.

# A $e^-e^+ \to e^-e^+$ Cross Section

The cross section is given by [8]:

$$
\begin{aligned}
\frac{d\sigma^{(1)}}{d\Omega}(\gamma(s),\gamma(s)) &= \frac{\alpha^2}{4s}(1+c^2) \\
\frac{d\sigma^{(2)}}{d\Omega}(Z(s),Z(s)) &= \frac{\alpha^2}{4s}|\chi(s)|^2((g_V^2+g_A^2)^2(1+c^2)+8g_V^2g_A^2c) \\
\frac{d\sigma^{(3)}}{d\Omega}(\gamma(s),Z(s)) &= \frac{\alpha^2}{4s}2\Re(\chi(s))(g_V^2(1+c^2)+2g_A^2c) \\
\frac{d\sigma^{(4)}}{d\Omega}(\gamma(t),\gamma(t)) &= \frac{\alpha^2}{4s}\frac{2}{(1-c)^2}((1+c^2)+4) \\
\frac{d\sigma^{(5)}}{d\Omega}(Z(t),Z(t)) &= \frac{\alpha^2}{4s}2\chi'(t)^2((g_V^2+g_A^2)^2((1+c^2)+4)+4g_V^2g_A^2((1+c^2)-4)) \\
\frac{d\sigma^{(6)}}{d\Omega}(\gamma(t),Z(t)) &= \frac{\alpha^2}{4s}4\chi'(t)\left((g_V^2+g_A^2)\frac{(1+c)^2}{(1-c)}+4(g_V^2-g_A^2)\frac{1}{(1-c)}\right) \\
\frac{d\sigma^{(7)}}{d\Omega}(\gamma(s),\gamma(t)) &= -\frac{\alpha^2}{4s}\frac{2(1+c)^2}{(1-c)} \\
\frac{d\sigma^{(8)}}{d\Omega}(Z(s),Z(t)) &= -\frac{\alpha^2}{4s}2\Re(\chi(s))\chi'(t)((g_V^2+g_A^2)^2+4g_V^2g_A^2)(1+c)^2 \\
\frac{d\sigma^{(10)}}{d\Omega}(\gamma(s),Z(t)) &= -\frac{\alpha^2}{4s}2\chi'(t)(g_V^2+g_A^2)(1+c)^2 \\
\frac{d\sigma^{(10)}}{d\Omega}(\gamma(t),Z(s)) &= -\frac{\alpha^2}{4s}2\Re(\chi(s))(g_V^2+g_A^2)\frac{(1+c)^2}{(1-c)}
\end{aligned}
$$

here $c$ denotes $\cos(\theta)$ and $\chi(s)$ and $\chi'(t)$ are given by:

$$\chi(s) = \frac{s}{s - M_Z^2 + \mathrm{i}\,\Gamma_Z M_Z}, \quad \chi'(t) = \frac{1}{2}\frac{s}{M_Z^2 - t}$$

# B Statistical Methods

In order to determine the error on binomial distributed random variables, we shall consider an example, following [9, p.21].

Lets assume a particle detector having detected $n = 9600$ out of $N = 11000$ particles. Furthermore, this process is assumed to be binomial distributed. The efficiency is then given by

$$\epsilon = \frac{n}{N} = 87.3\,\%$$

The statistical error on the efficiency is then given by

$$\Delta\epsilon = \sqrt{\frac{\epsilon(1-\epsilon)}{N}} = 0.3\,\% \tag{B.1}$$

Furthermore, we want to follow [10] and give a formula for the error propagation of an inverse matrix.

To this end, we assume an efficiency matrix given by

$$\varepsilon_{ij} = \frac{n_{ij}}{N_j}$$

where $n_{ij}$ denotes the number of remaining events of the sample $j$ upon applying the cuts $i$ and $N_j$ is the total number of events in the sample $j$. All $\varepsilon_{ij}$ are then positive definite and less than or equal to one. For the inverse matrix, the errors can then be determined via

$$[\Delta(\varepsilon^{-1})]_{ij} = \left|[\varepsilon^{-1}]_{im}[\Delta\varepsilon]_{mn}[\varepsilon^{-1}]_{nj}\right| \tag{B.2}$$

Following [11], we want to summarize how to calculate a weighted mean for physical measurements. Taking N measurements $x_1, \ldots, x_N$ with errors $\epsilon_1, \ldots, \epsilon_N$, the

weighted mean is defined as

$$x_{\mathrm{m}} = \frac{\sum_{i=1}^{N} w_i x_i}{\sum_{i=1}^{N} w_i} \quad \text{where} \quad w_i = \frac{1}{\sigma_i^2}. \tag{B.3}$$

The error on this mean is given by

$$\epsilon_m = \frac{1}{\sqrt{\sum_{i=1}^{N} w_i}}. \tag{B.4}$$

Peculiarly is here, that with the weights defined like this, more precise measurements count more than less precise measurements.

# C Figures

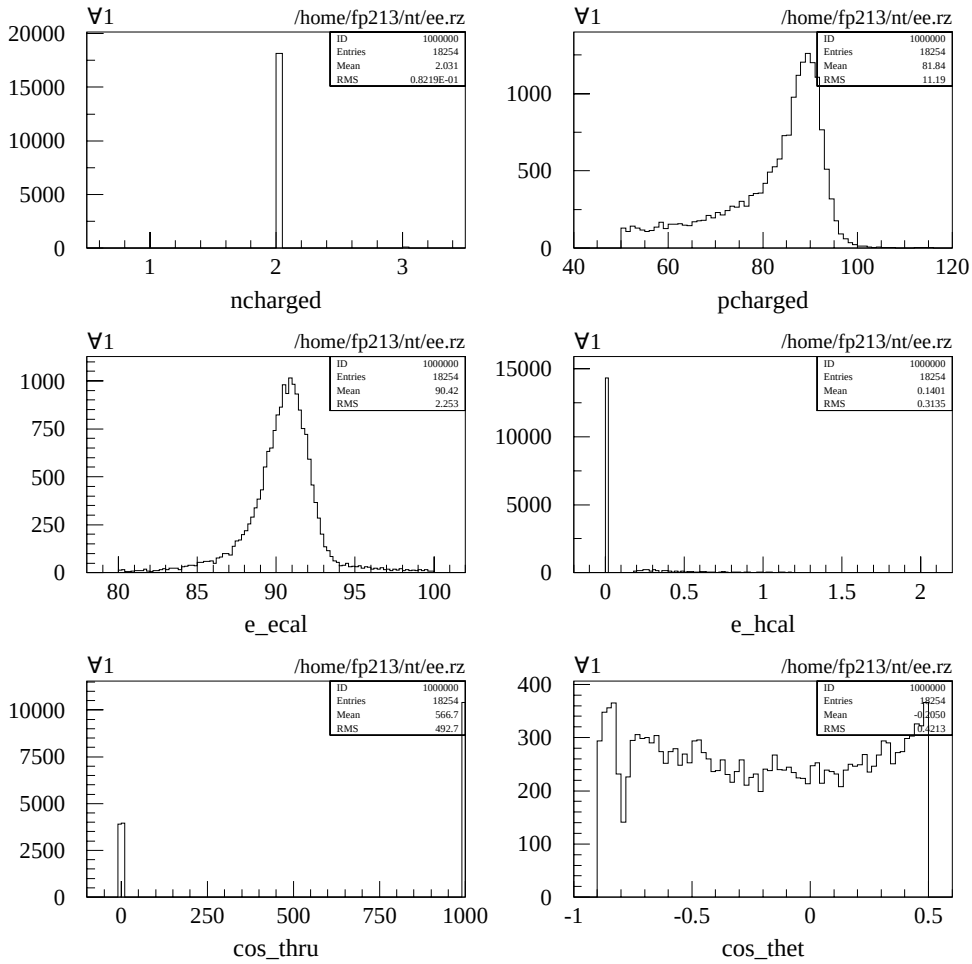


Figure C.1.: The histograms showing the variables of the electron sample after applying the cuts.

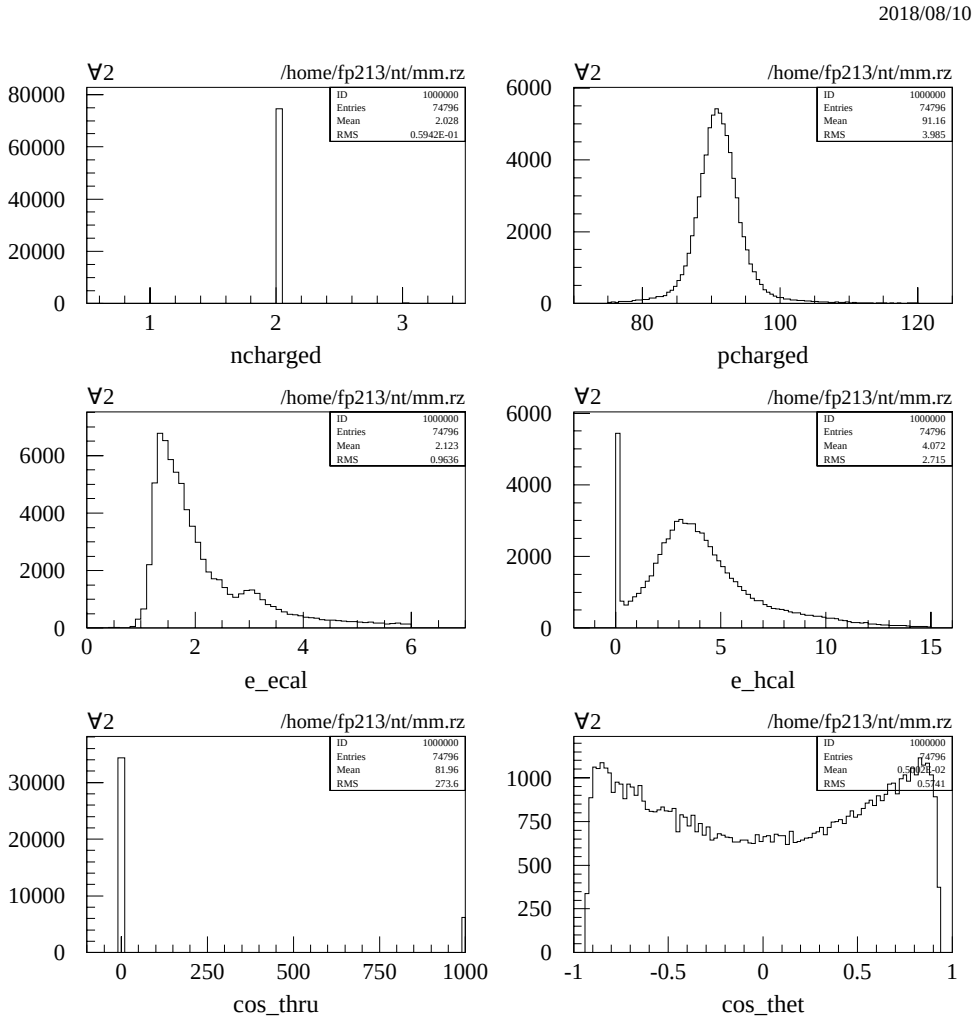


Figure C.2.: The histograms showing the variables of the muon sample after applying the cuts.

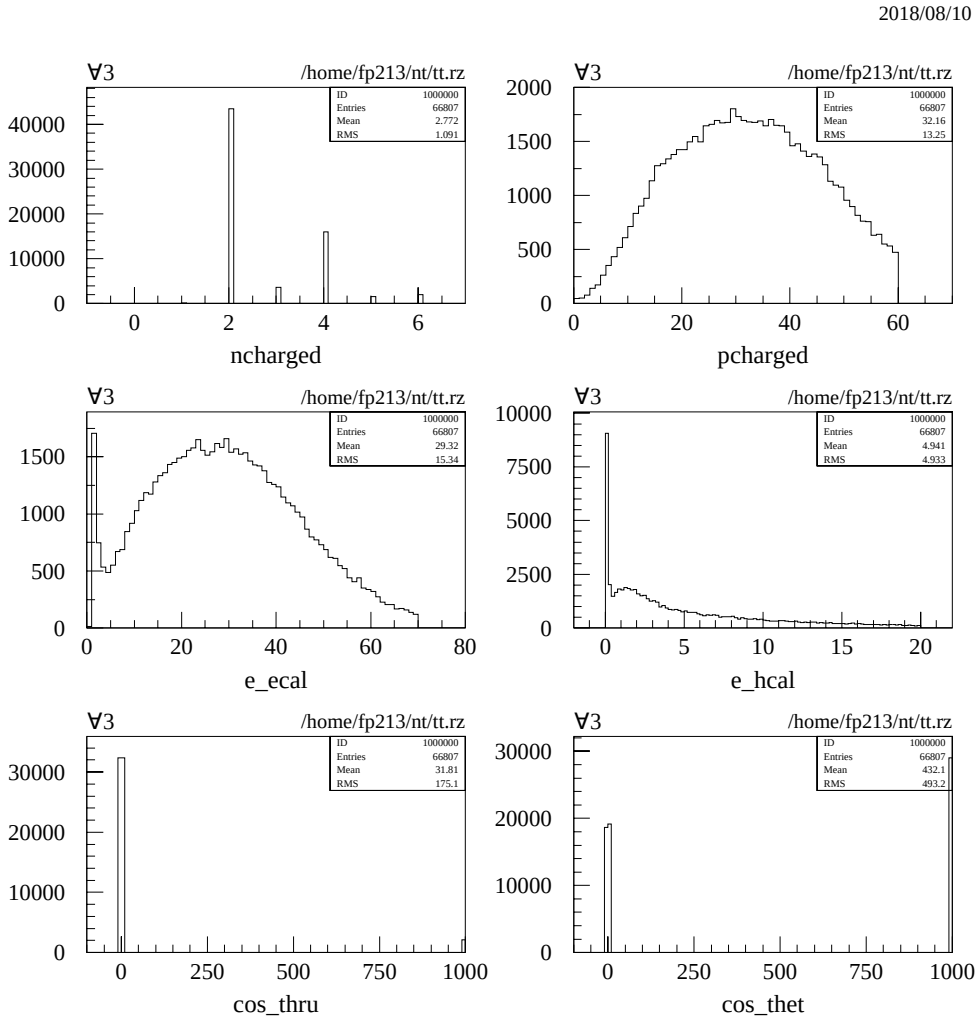


Figure C.3.: The histograms showing the variables of the tauon sample after applying the cuts.

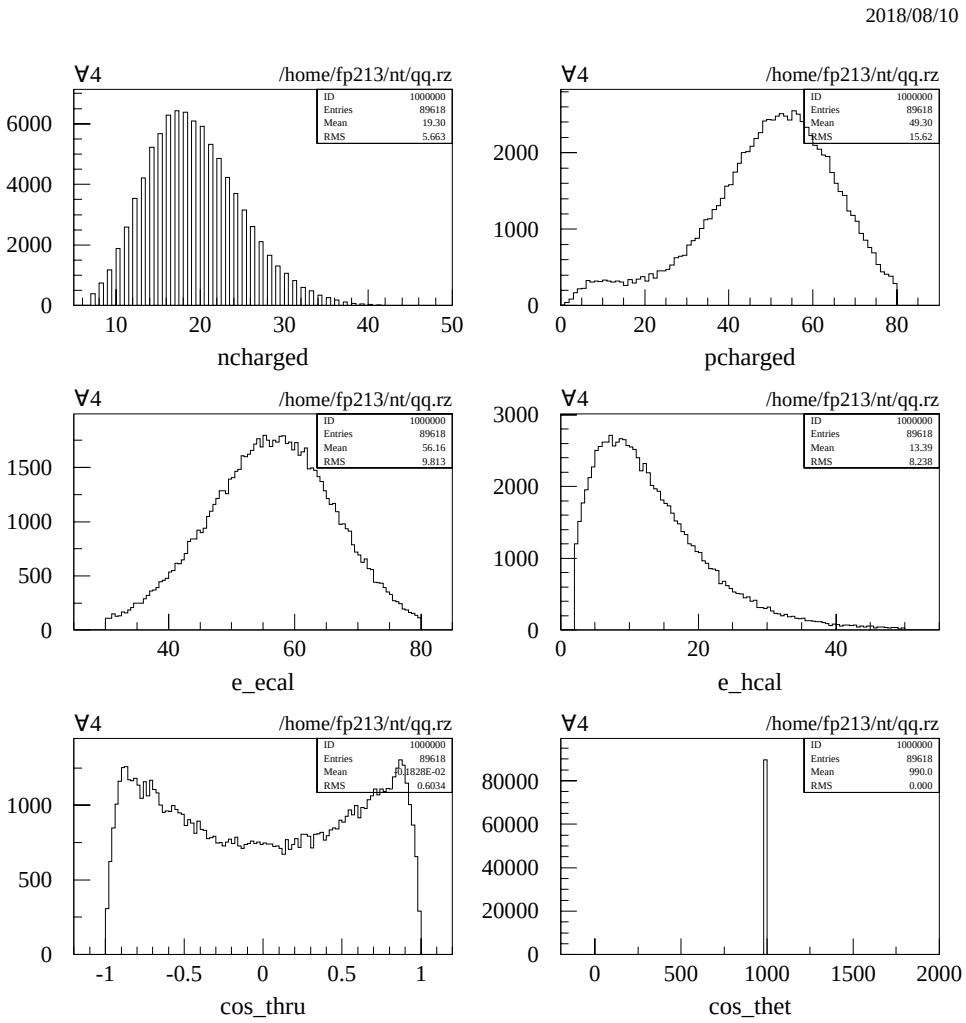


Figure C.4.: The histograms showing the variables of the hadron sample after applying the cuts.

# Bibliography

[1] W. R. Leo *Techniques for Nuclear and Particle Physics* Springer Verlag, 1987

[2] University of Bonn. *Advanced Physics Laboratory Course Part II, Instructions for E213 Analysis of $Z^0$ decays*. (English and German version).

[3] Carsten Burgard. Example: Standard model of physics.
`http://www.texample.net/tikz/examples/model-physics`.

[4] M. Drees, R. M. Godbole and P. Roy. *Theory and Phenomenology of Sparticles*. World Scientific Publishing Co. Pte. Ltd., 2004.

[5] M. E. Peskin and D. V. Schroeder. *An Introduction to Quantum Field Theory*. Westview Press, 2016.

[6] C. Patrignani et al. (Particle Data Group), Chin. Phys. C, 40, 100001 (2016) and 2017 update.

[7] University of Bonn. *Advanced Laboratory Course (physics601), Description of Experiments: E213 Analysis of $Z^0$ decays*. (Blue booklet). January 2015.

[8] TH Aachen, Dissertation Christoph Schäfer. Measurement of Bhabha Scattering at Center-of-Mass Energies between 89 GeV and 183 GeV with the L3 Detector at LEP.
`arXiv:hep-ex/9909031`.

[9] RWTH Aachen, Thomas Hebbeker. Vorbereitungskurs F-Praktikum B (Physik)
`https://web.physik.rwth-aachen.de/~hebbeker/lectures/stat_fprakt_1.pdf`.

[10] M. Lefebvre, R.K. Keeler, R. Sobie and J. White. Propagation of Errors for Matrix Inversion.
`arXiv:hep-ex/9909031`.

[11] University of Colorado, Minhyea Lee. PHYS2150 Experimental Physics, Spring 2018
`https://www.colorado.edu/physics/phys2150/phys2150_sp14/phys2150_lec4.pdf`.